

# Quantum-Classical Hybrid Quantized Neural Network

Wenxin Li<sup>1\*</sup>, Chuan Wang<sup>2†</sup>, Hongdong Zhu<sup>1</sup>, Qi Gao<sup>1</sup>, Yin Ma<sup>1</sup>, Hai Wei<sup>1</sup>, Kai Wen<sup>1‡</sup>

<sup>1</sup>Beijing QBoson Quantum Technology Co., Ltd., Beijing 100015, China

<sup>2</sup>School of Artificial Intelligence, Beijing Normal University, Beijing 100875, China

June 26, 2025

## Abstract

Here in this work, we present a novel Quadratic Binary Optimization (QBO) model for quantized neural network training, enabling the use of arbitrary activation and loss functions through spline interpolation. We introduce Forward Interval Propagation (FIP), a method designed to tackle the challenges of non-linearity and the multi-layer composite structure in neural networks by discretizing activation functions into linear subintervals. This approach preserves the universal approximation properties of neural networks while allowing complex nonlinear functions to be optimized using quantum computers, thus broadening their applicability in artificial intelligence. We provide theoretical upper bounds on the approximation error and the number of Ising spins required, by deriving the sample complexity of the empirical risk minimization (ERM) problem, from an optimization perspective. A significant challenge in solving the associated Quadratic Constrained Binary Optimization (QCBO) model on a large scale is the presence of numerous constraints. When employing the penalty method to handle these constraints, tuning a large number of penalty coefficients becomes a critical hyperparameter optimization problem, increasing computational complexity and potentially affecting solution quality. To address this, we employ the Quantum Conditional Gradient Descent (QCGD) algorithm, which leverages quantum computing to directly solve the QCBO problem. We prove the convergence of QCGD under a quantum oracle with randomness and bounded variance in objective value, as well as under limited precision constraints in the coefficient matrix. Additionally, we provide an upper bound on the Time-To-Solution for the QCBO solving process. Experimental results using a coherent Ising machine (CIM) demonstrate a 94.95% accuracy on the Fashion MNIST classification task, with only 1.1-bit precision. Compared to classical quantization-aware training (QAT), post-training quantization (PTQ) methods and full precision model, our approach yields higher accuracy, faster training, demonstrating its overall efficiency. In addition, evaluations against full-precision models show significant improvements in memory efficiency and inference latency, with minimal accuracy degradation. We further validate the robustness of the spline interpolation method and analyze the impact of varying precision levels on QCGD convergence, underscoring the reliability of our framework.

## Introduction

In recent years, the rapid progress of deep learning has catalyzed significant advances in a wide array of domains, from natural language processing [1] to computer vision [2], allowing intelligent systems to permeate our daily lives through devices such as smartphones [3] and autonomous vehicles [4]. However, the computational complexity and resource demands of deep neural networks (DNNs), typically trained and executed in high-precision floating-point arithmetic (e.g., 32-bit FP32), pose significant challenges for deployment in resource-constrained environments [5]. Neural network quantization has emerged as a pivotal technique to address these challenges by converting high-precision floating-point weights and activations into lower-precision formats, reducing memory usage, computational demands, and energy consumption with minimal accuracy loss [6]. This technique enables DNNs to operate effectively on resource-limited edge devices such as smartphones [7].

---

\*Email: liwx@boseq.com

†Corresponding Author. Email: wangchuan@bnu.edu.cn

‡Corresponding Author. Email: wenk@boseq.com

However, training quantized neural networks presents unique challenges despite their efficiency in inference. Unlike conventional deep neural networks, which rely on gradient-based optimization in a continuous domain, quantized models require solving a discrete optimization problem. The quantization process restricts the weights and activations to a predefined set of discrete values, resulting in a combinatorial search space and landscape [8]. To overcome these issues, studies on quantized neural network training focused primarily on two approaches: post-training quantization (PTQ) and quantization-aware training (QAT) [8]. PTQ transforms a pre-trained full-precision model into a low-bit representation by applying techniques such as range calibration or adaptive rounding, exemplified by AdaRound [9]. This method is computationally efficient but tends to suffer from significant accuracy loss under aggressive quantization, particularly at 4-bit precision or lower. In contrast, QAT integrates quantization effects during training, leveraging simulated quantization operations and the straight-through estimator (STE) to improve accuracy in low-precision scenarios [10]. Despite its advantages, QAT relies on heuristic approximations to circumvent the challenges posed by discrete optimization, limiting its ability to fully exploit the combinatorial structure of the problem.

These limitations highlight the need for a different approach to training quantized neural networks—one capable of efficiently navigating the discrete optimization landscape. The Ising machine [11, 12, 13, 14, 15, 16, 17] offers a promising avenue to address this challenge. By leveraging the energy-minimization properties of Ising models, researchers have applied Ising machines to train neural networks and perform statistical sampling [18]. For example, photonic Ising machines have demonstrated capabilities in low-rank combinatorial optimization and statistical learning tasks [19]; Equilibrium propagation using Ising machines has been utilized as a biologically plausible alternative to backpropagation for training neural networks effectively [20], and sparse Ising machines have been employed to train deep Boltzmann networks [21]. Using the principles of quantum coherence and Ising spin dynamics, these systems offer a unique approach to efficiently solving optimization problems central to neural network training, as well as in other fields such as wireless communication and signal processing [22, 23], molecular docking [24], computer vision [25, 26, 27, 28, 29, 30], etc.

In neural network training, the selection of the activation function critically influences the performance of the model and the adaptability to the task [31]. While the simplicity and computational efficiency of Rectified Linear Units (ReLU) make them suitable for many applications, certain scenarios demand the distinctive non-linear characteristics of sigmoid or hyperbolic tangent (tanh) functions. Restricting the network to a specific activation function limits its expressive power and adaptability, potentially leading to suboptimal performance on certain tasks. Consequently, the development of training methodologies capable of supporting diverse activation functions becomes essential, as this versatility allows neural networks to effectively address broader problem domains and dataset characteristics, thereby significantly enhancing their practical applicability. A pioneering effort in this domain is the complete quantum neural network (CQNN) framework [32], which implements a comprehensive neural network architecture encompassing weights, biases, activation functions, and loss minimization within a quantum annealing system. This approach achieves the training in a single annealing step, offering notable advantages, including guaranteed convergence to global optima and substantially reduced training durations, in stark contrast to the iterative optimization process characteristic of conventional gradient descent methods.

However, a critical limitation of CQNN emerges in its handling of activation functions. To conform to the quadratic constraints of the Ising model Hamiltonian, CQNN approximates arbitrary activation functions (e.g., ReLU, sigmoid) with polynomials. This choice raises concerns rooted in approximation theory. As established by Leshno et al. [33], multilayer feedforward networks with non-polynomial activation functions are dense in the space of continuous functions between Euclidean spaces under the compact convergence topology, a property ensuring universal approximation capability. Polynomial activation functions, conversely, limit this expressiveness, as they form a finite-degree polynomial space incapable of approximating arbitrary continuous functions [33, 34]. In addition to the limitations in expressive power, another significant drawback arises when constructing QUBO models is, polynomial activation functions require a large number of Ising spins for degree reduction. This issue further exacerbates the challenges of applying CQNN in practical scenarios. Therefore, adapting arbitrary, non-polynomial activation functions to quantum computing frameworks remains an open challenge, requiring innovative encoding strategies or hybrid quantum-classical solutions to preserve both computational efficiency and model versatility.

When addressing constrained quadratic optimization problems, the penalty method is frequently used to incorporate constraints into the objective function [35]. However, this approach has significant limitations.

First, quadratic penalty functions introduce pairwise interactions among all variables, transforming sparse problems into fully connected ones. This increased connectivity requires complex mapping techniques, particularly for quantum annealers with limited connectivity [36], substantially raising resource demands on near-term quantum hardware [37]. Second, quadratic penalties generate large energy scales that can exceed hardware dynamic ranges, necessitating Hamiltonian normalization [37]. This normalization reduces the problem’s effective energy resolution, impairing optimization performance. Additionally, the penalty method alters the optimization landscape, requiring careful tuning of penalty coefficients, a critical hyperparameter for effective constraint handling. As the number of constraints grows, the search space for optimal penalty coefficients expands exponentially, posing a significant challenge to achieving robust optimization outcomes.

In this study, we present a framework for training quantized neural networks using CIM. Our approach begins by formulating the quantization training problem as a QUBO problem and then leveraging quantum algorithms to overcome the shortcomings of existing methods of training quantized neural networks. Furthermore, we derive a sample complexity bound from an optimization perspective, effectively constraining the number of spins required in the quadratic binary model. This bound lays a critical foundation for scaling to large-scale scenarios by ensuring computational feasibility and efficiency. Our experimental evaluation highlights the effectiveness of this approach across multiple dimensions. Compared to standard quantization-aware training (QAT) methods, our method achieves higher accuracy with training times reduced by several orders of magnitude. When evaluated against post-training quantization (PTQ) algorithms, it delivers superior accuracy with fewer parameter bits—achieving 94.95% accuracy with only 1.1-bit precision. Furthermore, compared to full-precision models with continuous weights, our quantized networks significantly reduce memory footprint and inference latency while maintaining competitive accuracy. These results demonstrate the potential of quantum optimization to enable efficient and high-performing deep learning models for edge deployment, and paves the way for the next generation of efficient deep learning systems.

## Results

### Principle

The approach first conceptualizes a quantized neural network (QNN) as a parameterized operator  $\mathcal{Q} : \mathbb{R}^d \rightarrow \mathbb{R}$ , which transforms an input space  $\mathbb{R}^d$  into the output space  $\mathbb{R}$  through a parameter set  $\mathcal{W}$  drawn from a discrete parameter space. This operator emerges from a hierarchical cascade of quantized transformations, reflecting the network’s layered and constrained architecture.

The global operator  $\mathcal{Q}(x, \mathcal{W})$  could be expressed as a nested sequence of  $L$  quantized layers:

$$\mathcal{Q}(x, \mathcal{W}) = \mathcal{Q}_L(\mathcal{Q}_{L-1}(\cdots \mathcal{Q}_1(x, \mathcal{W}_1), \mathcal{W}_2) \cdots, \mathcal{W}_L), \quad (1)$$

where  $L$  denotes the depth of the network, and  $\mathcal{W}$  encompasses the quantized parameters across all layers. For each layer  $l$  ( $1 \leq i \leq L$ ), the parameter set  $\mathcal{W}_l = (\mathbf{W}_l, \mathbf{b}_l)$  consists of a quantized weight matrix  $\mathbf{W}_l$  and a quantized bias vector  $\mathbf{b}_l$ , with dimensional compatibility where the input dimension at layer 1 is  $d$  and the output dimension at layer  $L$  is 1.

Each layer’s transformation  $\mathcal{Q}_l$  operates on the quantized output of the previous layer via the transform as:

$$\mathcal{Q}_l(x, \mathcal{W}_l) = \sigma(\mathbf{W}_l \cdot x + \mathbf{b}_l), \quad (2)$$

where  $\sigma : \mathbb{R} \rightarrow \mathbb{R}$  denotes the non-linear activation function applied elementwise, and the operation  $\cdot$  reflects a quantized linear combination.

The activation value of the  $j^{\text{th}}$  neuron in the  $l^{\text{th}}$  layer is related to the activation values of the  $(l - 1)^{\text{th}}$  layer through the following formula:

$$a_{l,j} = \sigma\left(\sum_k w_{ljk} a_{l-1,k} + b_{lj}\right). \quad (3)$$

Here, the sum of  $k$  is taken over all the neurons in the  $(l - 1)$ -th layer.

Figure 1 illustrates the workflow of the quantized neural network training framework, using the hybrid approach and CIM. The process begins with data preparation and progresses through the formulation of the loss landscape and solution space of a hypercube structure. Key steps include the constraint linearization, the transformation of the problem into a QCBO model, and the iterative solution process using an Ising machine. Variables are updated based on the QUBO matrix at each iteration, ensuring convergence toward the optimal solution. Therefore, this work can achieve marked performance in quantum computing in real-world applications, laying a solid foundation for using quantum computing in QNN training.

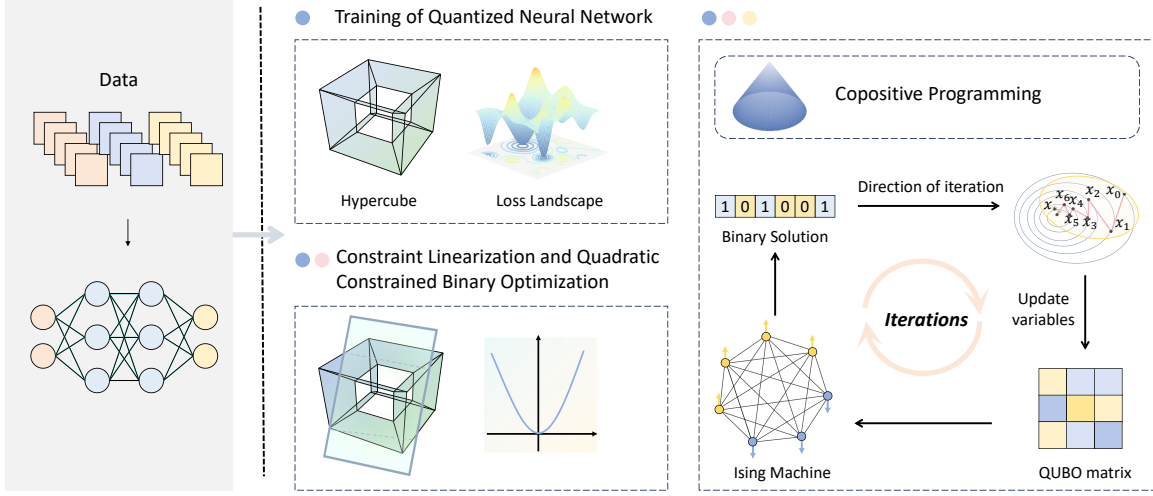


Figure 1: The flowchart of the quantized neural network training process using CIM and hybrid techniques.

## Spline-Induced Neural Network and Optimization Landscape

The piecewise linear functions are adopted as the activation functions in the neural network. These functions are particularly advantageous due to their simplicity and computational efficiency, while still maintaining the ability to approximate complex, non-linear relationships, as shown in the following fact.

**Fact 1 ([38, 39])** For any function  $f \in \mathcal{F}_{d,n} = \mathcal{W}^{n,\infty}([0, 1]^d)$  (where  $d$  is the input dimension,  $n$  is the order of weak derivatives, and  $\max_{\mathbf{n}:|\mathbf{n}|\leq n} \text{ess sup}_{\mathbf{x} \in [0,1]^d} |D^{\mathbf{n}} f(\mathbf{x})| \leq 1$ ), and any error bound  $\epsilon \in (0, 1)$ , there exists a quantized neural network  $f_q$  with any piecewise linear activation function having a finite number of breakpoints and weights restricted to  $\lambda \geq 2$  discrete values, such that:

$$|f(\mathbf{x}) - f_q(\mathbf{x})| \leq \epsilon, \quad \forall \mathbf{x} \in [0, 1]^d \quad (4)$$

The number of weights required by  $f_q$  has an upper bound of  $\mathcal{O}(\lambda \log^{\frac{1}{\lambda-1}+1}(1/\epsilon)(1/\epsilon)^{d/n})$ , while an unquantized piecewise linear neural network  $f_u$  with the same activation function achieving the same error has an upper bound of  $\mathcal{O}(\log(1/\epsilon)(1/\epsilon)^{d/n})$ . Thus, the quantized weight count exceeds the unquantized one by a factor of  $\mathcal{O}(\log^5(1/\epsilon))$ , which is significantly smaller than the lower bound for unquantized network,  $\Omega(\log^{-3}(1/\epsilon)(1/\epsilon)^{d/n})$ .

This fact confirms that a quantized piecewise linear neural network, regardless of the specific activation, approximates target functions with efficiency comparable to an unquantized one, incurring only a low complexity overhead. Ding et al. [38] further reveal a theoretical optimal number of discrete weight values, typically lies between 1 and 4 bits across a wide range of  $d$  and  $\epsilon$ , indicating that effective quantization of piecewise linear neural network requires only a small number of discrete weights. The efficiency supports the use of quantized piecewise linear neural networks in quantum computing contexts, where minimal discrete states could leverage quantum parallelism for training.

While Fact 1 establishes the universal approximation capability of quantized piecewise linear neural networks, it remains an interesting question to quantify the approximation error introduced when replacing a smooth activation function with a piecewise linear one, especially in the presence of spectral normalization, which is often employed to control model complexity and improve generalizability [40]. In this work, we present the following theorem to provide the error bound induced by piecewise linear approximations in a feedforward neural network.

**Theorem 1** Consider an  $L$ -layer feedforward neural network  $f : \mathbb{R}^d \rightarrow \mathbb{R}^m$ , where  $W_l \in \mathbb{R}^{m_l \times m_{l-1}}$  represents the weight matrix in the  $l$ -th layer, and is spectrally normalized [40].  $\sigma : \mathbb{R} \rightarrow \mathbb{R}$  is Lipschitz continuous with constant  $L_\sigma \leq 1$ . Let  $\hat{f}$  denote the network with  $\sigma$  replaced by a piecewise linear function  $\hat{\sigma}$ , satisfying:

$$\sup_{z \in \mathbb{R}} |\sigma(z) - \hat{\sigma}(z)| \leq \epsilon_\sigma, \quad (5)$$

and Lipschitz constant  $L_{\hat{\sigma}} \leq 1$ . Assume inputs  $x \in \mathcal{X} \subset \mathbb{R}^d$  satisfy  $\|x\|_2 \leq B$ , and each layer has  $m_l \leq m$  neurons. Then:

$$\sup_{x \in \mathcal{X}} \|f(x) - \hat{f}(x)\|_2 \leq \epsilon_\sigma \sqrt{m} L. \quad (6)$$

If  $\sigma$  is twice continuously differentiable with  $\|\sigma''\|_\infty \leq M$ , the number of segments  $n$  in  $\hat{\sigma}$  to achieve an error no more than  $\epsilon$  scales as:

$$n = O\left(\frac{1}{\sqrt{\epsilon}}\right). \quad (7)$$

The proof of Theorem 1 is provided in the supplementary material. This result and analysis provide insight into the trade-offs between model efficiency and approximation accuracy, particularly relevant in the context of quantum-enhanced neural network training.

The objective of training can be formulated as a discrete optimization problem over the parameter space, aiming to minimize a generalized loss function evaluated across the entire input distribution  $x$ :

$$\min_{\mathcal{W} \in \mathcal{W}_{\text{quant}}} \sum_x \mathcal{L}(a_x^L, y_x), \quad (8)$$

subject to the quantized layer dynamics:

$$a_x^l = \sigma(z_x^l), \quad \forall x, 1 \leq l \leq L, \quad (9)$$

$$z_x^l = \mathbf{W}_l \cdot a_x^{l-1} + \mathbf{b}_l, \quad \forall x, 1 \leq l \leq L, \quad (10)$$

where  $a_x^0 = x$  serves as the input,  $a_x^L$  is the quantized network output,  $y_x$  represents the target output, and  $\mathcal{W}_{\text{quant}}$  denotes the set of all permissible quantized parameter configurations. This formulation captures the trade-offs between accuracy and computational efficiency inherent in quantization.

**Forward Interval Propagation.** Activation functions play a crucial role in neural networks by introducing nonlinearities that enable complex mappings between inputs and outputs. We leverage spline approximation with piecewise constant functions to approximate activation and loss functions, such as mean squared error (MSE), cross-entropy loss, and Huber loss, which quantify the difference between predicted and actual values in machine learning tasks.

Forward Interval Propagation (FIP) is designed to address the challenges of non-linearity in neural networks, particularly the complex multi-layer composite relationships inherent in activation functions. Also, FIP is to simplify these complex interactions by discretizing the activation function into multiple linear subintervals. This allows for efficient computation while preserving the expressive power of neural networks. As shown in Figure 2, we divide the entire value range into multiple subintervals. The activation function is defined as a piecewise function, where the output of each neuron is determined by the specific subinterval it belongs to. The summation of these outputs, along with the bias term, determines the subinterval for the output of the next layer. This process is repeated during forward propagation, establishing a relationship between the input and output by propagating through the defined subintervals.

One of the key benefits of FIP is its ability to capture and manage the multi-layer composite relationships in neural networks. As the forward propagation proceeds, the activation functions at each layer are constrained to a specific subinterval, and the overall relationship between input and output is effectively captured by the combination of these subintervals.

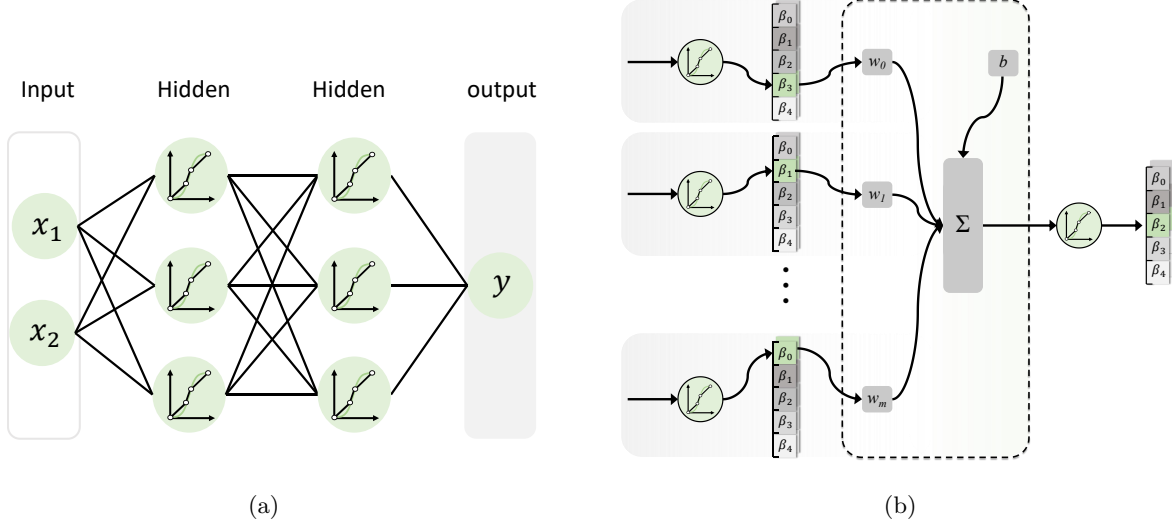


Figure 2: (a) Feedforward neural network with piecewise linear activation function. (b) Schematic representation of forward interval propagation (FIP) in a neural network, illustrating the discretization of activation functions into linear subintervals. The diagram shows multiple input neurons (left) connected through weights ( $w_0, w_1, \dots, w_m$ ) and a bias term  $b$  to a summation node  $\Sigma$ , followed by an activation function. The green highlighted intervals and values of  $\beta_i$ s indicate the specific subintervals that the activation function's output values belong to, determining the output subinterval for the next layer, effectively capturing multi-layer composite relationships during forward propagation.

We divide the interval  $[\underline{M}, \overline{M}]$  as  $\underline{M} = M_0 \leq M_1 \leq M_2 \leq \dots \leq M_n = \overline{M}$ , And the neural network training problem could be formulated as the following QCBO expression:

$$\begin{aligned}
& \sum_x \sum_{i=1}^{n+1} \beta_{a_x^L}^{(i-1)} \cdot \mathcal{L}_x(M_{i-1}, y_x) \\
& s.t. a_{x,j}^l = \sum_{i=1}^{n+1} \beta_{z_{x,j}^L}^{(i-1)} \cdot (\sigma(M_{i-1}) + \sigma(M_i))/2, \forall x, j, l \\
& \sum_{i=1}^n \beta_{a_x^L}^{(i)} M_{i-1} \leq a_x^L \leq \sum_{i=1}^n \beta_{a_x^L}^{(i)} M_i, \forall x \\
& \sum_{i=1}^n \beta_{z_{x,j}^L}^{(i)} M_{i-1} \leq \sum_k w_{jk}^l a_{x,k}^{l-1} + b_j^l \leq \sum_{i=1}^n \beta_{z_{x,j}^L}^{(i)} M_i, \forall x, j, l \\
& \sum_{i=1}^n \beta_{a_x^L}^{(i)} = 1, \forall x, \sum_{i=1}^n \beta_{z_{x,j}^L}^{(i)} = 1, \forall x, j, l
\end{aligned} \tag{11}$$

where  $x, y_x$  represents the label,  $a_x^L$  denotes the output of the last layer;  $a_{x,j}^l$  denotes the output of the  $j$ -th neuron of the  $l$ -th layer;  $C(M_i, y_x)$  indicates the the loss when the last layer's output is in the  $i$ -th subinterval and the target is  $y_x$ . For any variable  $\tau$ ,  $\beta_\tau = 1$  if  $\tau$  lies within the  $i$ -th sub-interval and 0 otherwise.

Note that  $w_{jk}^l a_{x,k}^{l-1}$  contains quadratic terms, which will introduce higher-order terms when transformed into the QUBO form. Therefore, it is necessary to perform a reduction operation to the lower order. For example, when using the penalty method to obtain the QUBO model, we can replace the term  $x_1 x_2$  by a

binary variable  $y$  and add the Rosenberg polynomial [41]  $h(x_1, x_2, y) = 3y + x_1x_2 - 2y(x_1 + x_2)$ , to the objective function. These auxiliary variables help to linearize the expression, making it easier to handle.

In addition, the non-binary variables  $a_{x,j}^l, w_{jk}^l, b_j^l$  are represented using binary encoding as following:  $a_{x,j}^l = \sum_{\ell} 2^{\ell} \cdot \delta_{a_{x,k}^l}^{(\ell)}, w_{jk}^l = \sum_{\ell} 2^{\ell} \cdot \delta_{w_{jk}^l}^{(\ell)}, b_j^l = \sum_{\ell} 2^{\ell} \cdot \delta_{b_j^l}^{(\ell)}$ . In supplementary, we also provide the details of the QCBO model when spline approximation with piecewise linear functions is used.

**Spin Complexity and Upper Bounds.** Table 1 summarizes the required number of ising spins for various variables in our quadratic programming model, showing that the overall number of ising spins required is  $O(nWDN)$ , for handling the datasets with  $N$  samples and the neural network with width  $W$  and depth  $D$ .

Variable	Required Number of ising spins
$\beta_x^{(i)}$	$O(nWDN)$
$w_{jk}^l$	$O(DW^2)$
$b_j^l$	$O(WD)$
$a_{x,j}^l$	$O(WDN)$
Linearization	$O(nWDN)$

Table 1: The number of required ising spins for each variable

Recall that our objective is to minimize:

$$\mathcal{L}(\theta) = \mathbb{E}_{(x,y_x) \sim \mathcal{D}}[C_x(f_{\theta}(x), y_x)], \quad (12)$$

where  $\theta = \{w^l, b^l\}_{l=1}^L, f_{\theta}(x) = a_x^L$ . We solve empirical risk minimization (ERM) over  $N$  i.i.d. samples  $\{(x_i, y_i)\}_{i=1}^N \sim \mathcal{D}$ :

$$\hat{\theta}_N = \arg \min_{\theta \in \Theta} \hat{\mathcal{L}}_N(\theta) = \frac{1}{N} \sum_{i=1}^N C_{x_i}(f_{\theta}(x_i), y_i).$$

Note that the number of samples  $N$  can be bounded while ensuring the efficiency of our learning process, this is where the concept of VC dimension becomes crucial.

**Lemma 1** ([42, 43]) *The VC dimension of a neural network with piecewise polynomial activation functions is bounded by  $O(W^3D^2)$ . Specifically, when the activation functions are piecewise constant, the VC dimension is no more than  $O(W^2D(\log W + \log D))$ .*

Within the *Probably Approximately Correct* (PAC) learning framework [44], the focus is on controlling the *generalization error* [44], a measure of how accurately an algorithm is able to predict outcomes for previously unseen data. This framework ensures that, with high probability  $1 - \alpha$ , the generalization error is confined within a precision  $\varepsilon$ . Consequently, the required number of samples can be bounded as:

$$N = O\left(\frac{\text{VCdim}}{\varepsilon} \log \frac{1}{\alpha}\right) = O\left(\frac{W^2D(\log W + \log D)}{\varepsilon} \log \frac{1}{\alpha}\right). \quad (13)$$

Moreover, from an optimization perspective, we can derive a sample complexity bound tailored to the optimization error, defined as the discrepancy between the expected loss of the learned parameters and the minimum loss, i.e.,  $\mathcal{L}(\hat{\theta}_N) - \mathcal{L}(\theta^*)$ . This focus on optimization error is particularly pertinent given that our study is about addressing optimization problems,

**Theorem 2** *For a quantized neural network with  $B$ -bit parameters, let  $\varepsilon, \alpha \in (0, 1)$ , and assume the loss function  $C_x(\cdot)$  is bounded in  $[0, C_{\max}]$ . Then, with probability at least  $1 - \alpha$ ,*

$$\mathcal{L}(\hat{\theta}_N) \leq \mathcal{L}(\theta^*) + \varepsilon, \quad (14)$$

provided  $N = O\left(\frac{C_{\max}^2}{\varepsilon^2} \log \frac{|\Theta|}{\alpha}\right)$ . Substituting  $|\Theta|$ :

$$N = O\left(\frac{C_{\max}^2}{\varepsilon^2} \sum_{l=1}^L d_l(d_{l-1} + 1)B \log 2 + \log \frac{1}{\alpha}\right), \quad (15)$$

where  $d_l$  and  $d_{l-1}$  are the layer dimensions.

**Proof:** Define the function class  $\mathcal{G} = \{g_\theta(x, y) = C_x(f_\theta(x), y) : \theta \in \Theta\}$ . Given the finite  $\Theta$ , apply Hoeffding's inequality for  $g_\theta \in [0, C_{\max}]$ :

$$P\left(\left|\frac{1}{N} \sum_{i=1}^N g_\theta(x_i, y_i) - \mathbb{E}_{(x, y_i)}[g_\theta(x_i, y_i)]\right| > \varepsilon/2\right) \leq 2 \exp\left(-\frac{2N\varepsilon^2}{C_{\max}^2}\right). \quad (16)$$

Using a union bound over all  $|\Theta|$  functions:

$$P\left(\sup_{\theta \in \Theta} \left|\frac{1}{N} \sum_{i=1}^N g_\theta(x_i, y_i) - \mathbb{E}_{(x, y_i)}[g_\theta(x_i, y_i)]\right| > \varepsilon/2\right) \leq 2|\Theta| \exp\left(-\frac{2N\varepsilon^2}{C_{\max}^2}\right). \quad (17)$$

Set the probability to  $\alpha$ , i.e.,  $2|\Theta| \exp\left(-\frac{2N\varepsilon^2}{C_{\max}^2}\right) \leq \alpha$ , we have  $N \geq \frac{C_{\max}^2}{2\varepsilon^2} \log \frac{2|\Theta|}{\alpha}$ . Since  $\hat{\theta}_N$  minimizes  $\hat{\mathcal{L}}_N$ :

$$\mathcal{L}(\hat{\theta}_N) \leq \hat{\mathcal{L}}_N(\hat{\theta}_N) + \varepsilon/2 \leq \hat{\mathcal{L}}_N(\theta^*) + \varepsilon/2 \leq \mathcal{L}(\theta^*) + \varepsilon. \quad (18)$$

Since the total number of configurations is  $|\Theta| \leq \prod_{l=1}^L (2^B)^{d_l(d_{l-1}+1)}$ . The proof is complete by substituting  $|\Theta|$ . □

## Noise-Robust Hybrid Dynamics

In this section, we confront the formidable optimization challenges stemming from the proliferation of constraints in large-scale networks in the aforementioned model. The abundance of constraints not only complicates the optimization process but also necessitates the determination of numerous penalty coefficients in the traditional penalty method. The task of figuring out these penalty coefficients becomes increasingly intricate as the number of constraints grows, leading to potential inefficiencies and suboptimal solutions.

To surmount this hurdle, we use the *Quantum Conditional Gradient Descent* (QCGD) algorithm developed in [45], a cutting-edge hybrid classical-quantum framework tailored to address quadratic, linearly-constrained, binary optimization problems on quantum machines. Our workflow starts with data being fed into the neural network. The optimization problem is then formulated as a QCBO. This problem is subsequently linearized and transformed into a copositive programming problem. In the hybrid quantum-classical iterative process, during each iteration, the quantum conditional gradient method calculates the update direction by minimizing a linear approximation of the penalized proxy of the objective function. QCGD formulates the linear minimization problem as a QUBO sub-problem, which is suitable for Ising machines. CIM solves the QUBO problem, and the solution obtained is fed back into the classical computing step to calculate the direction of iteration. This iterative loop continues, with the QUBO matrix being updated at each step, until convergence towards an optimal solution is achieved.

In the following theorem, we prove that by sampling a certain number of solutions from the Ising machine at each iteration, the algorithm can still converge despite the presence of errors.

**Theorem 3** *Consider the Quadratic Constrained Binary Optimization (QCBO) problem solved using the Q-FW algorithm with a random quantum oracle. At step  $t$ , the error in the objective in a single run of the quantum oracle, has mean  $\mu_t$  and variance  $\sigma_t$ , both of which have time-independent upper bounds. Then:*

1. Q-FW algorithm converges to the optimal solution almost surely, i.e.,

$$\mathbb{P}(\lim_{t \rightarrow \infty} \mathbf{V}_t = \mathbf{V}^*) = 1. \quad (19)$$

2. In expectation, the objective gap and residual gap converge as:

$$\mathbb{E}[\text{Objective-gap}_T] = O\left(\frac{1}{\sqrt{T}}\right), \quad \mathbb{E}[\text{Infeasibility}_T] = O\left(\frac{1}{\sqrt{T}}\right) \quad (20)$$

3. The total time to solution for any fixed success probability satisfies:

$$TTS_{QCBO} = O(\tau \cdot T \cdot \log n), \quad (21)$$

where

- $m_t = c \log T + 1$  be the number of independent quantum samples per iteration  $t$ , with  $c = \frac{2}{-\log(1-p_0)}$ ,  $p_0 > 0$  the probability of the quantum oracle returning the optimal QUBO solution,
- $\tau$  is the time per quantum oracle call.

**Proof:** The subproblem in the  $t$ -th iteration is solved via  $m_t = c \log n$  repetitions, selecting the best solution among samples  $\{\mathbf{D}_t^{(i)}\}_{1 \leq i \leq m_t}$ , i.e.,  $\mathbf{D}_t = \mathbf{D}_t^{(i_t)}$ , where

$$i_t = \underset{1 \leq i \leq m_t}{\operatorname{argmin}} \operatorname{Tr}(\mathbf{Q}_{\text{QUBO}}^{(t)} \mathbf{D}_t^{(i)}). \quad (22)$$

For any  $r > 0$ , the  $r$ -th moment of quantum oracle error

$$\mathbb{E} \left[ \left( \operatorname{Tr}(\mathbf{Q}_{\text{QUBO}}^{(t)} \mathbf{D}_t) - \operatorname{Tr}(\mathbf{Q}_{\text{QUBO}}^{(t)} \mathbf{D}_t^*) \right)^r \right] \quad (23)$$

$$= \mathbb{P}(\mathbf{D}_t \neq \mathbf{D}_t^*) \cdot \mathbb{E} \left[ \left( \operatorname{Tr}(\mathbf{Q}_{\text{QUBO}}^{(t)} \mathbf{D}_t) - \operatorname{Tr}(\mathbf{Q}_{\text{QUBO}}^{(t)} \mathbf{D}_t^*) \right)^r \middle| \mathbf{D}_t \neq \mathbf{D}_t^* \right] \quad (24)$$

$$\leq \mathbb{P}(\mathbf{D}_t \neq \mathbf{D}_t^*) \cdot \mathbb{E} \left[ \left( \operatorname{Tr}(\mathbf{Q}_{\text{QUBO}}^{(t)} \mathbf{D}_t^{(i)}) - \operatorname{Tr}(\mathbf{Q}_{\text{QUBO}}^{(t)} \mathbf{D}_t^*) \right)^r \middle| \mathbf{D}_t \neq \mathbf{D}_t^* \right] \quad (25)$$

$$= \mathbb{P}(\mathbf{D}_t \neq \mathbf{D}_t^*) \cdot \mathbb{E} \left[ \left( \operatorname{Tr}(\mathbf{Q}_{\text{QUBO}}^{(t)} \mathbf{D}_t^{(i)}) - \operatorname{Tr}(\mathbf{Q}_{\text{QUBO}}^{(t)} \mathbf{D}_t^*) \right)^r \middle| \mathbf{D}_t^{(i)} \neq \mathbf{D}_t^* \right] \quad (26)$$

$$= \frac{\mathbb{P}(\mathbf{D}_t \neq \mathbf{D}_t^*)}{\mathbb{P}(\mathbf{D}_t^{(i)} \neq \mathbf{D}_t^*)} \cdot \mathbb{E} \left[ \left( \operatorname{Tr}(\mathbf{Q}_{\text{QUBO}}^{(t)} \mathbf{D}_t^{(i)}) - \operatorname{Tr}(\mathbf{Q}_{\text{QUBO}}^{(t)} \mathbf{D}_t^*) \right)^r \right], \quad (27)$$

where the second equality is based on the independence of samples. For  $m_t = c \log T$ ,

$$\frac{\mathbb{P}(\mathbf{D}_t \neq \mathbf{D}_t^*)}{\mathbb{P}(\mathbf{D}_t^{(i)} \neq \mathbf{D}_t^*)} = (1 - p_0)^{m_t - 1} = \frac{1}{T^2}, \quad (28)$$

we have

$$\mathbb{E} \left[ \operatorname{Tr}(\mathbf{Q}_{\text{QUBO}}^{(t)} \mathbf{D}_t) - \operatorname{Tr}(\mathbf{Q}_{\text{QUBO}}^{(t)} \mathbf{D}_t^*) \right] \leq \frac{\mu_t}{T^2}, \quad (29)$$

$$\operatorname{Var} \left[ \operatorname{Tr}(\mathbf{Q}_{\text{QUBO}}^{(t)} \mathbf{D}_t) - \operatorname{Tr}(\mathbf{Q}_{\text{QUBO}}^{(t)} \mathbf{D}_t^*) \right] \leq \frac{\sigma_t + \mu_t^2}{T^2}. \quad (30)$$

We next claim that  $\mu_t$  and  $\sigma_t$  is bounded, since

$$\operatorname{Tr}(\mathbf{Q}_{\text{QUBO}}^{(t)} \mathbf{D}_t) \leq \sum_{i,j} |Q_{ij}^{(t)}| = O(n^2), \quad (31)$$

which is independent of iteration index  $t$ , assuming each element in  $\mathbf{Q}_{\text{QUBO}}^{(t)}$  is constant. According to Proposition 1, we can get the order of convergence in expectation, and the almost sure convergence follows from the concentration probability bound that converges to 1 when  $T$  is infinity.

The bound on TTS can also be derived from the concentration result in Proposition 1. A more straightforward approach is based on the union bound, the probability that

$$\mathbb{P}(\exists t, \mathbf{D}_t \neq \mathbf{D}_t^*) \leq \sum_{t=1}^T \mathbb{P}(\mathbf{D}_t \neq \mathbf{D}_t^*) = \frac{1}{T} \quad (32)$$

Therefore, With high probability  $1 - \frac{1}{\text{poly}(n)} \geq p_R$ ,  $\mathbf{D}_t = \mathbf{D}_t^*$  for all  $t$ , yielding the convergence to optimal solution. As per-iteration time of Q-FW is  $m_t\tau$ , we can obtain the second conclusion for  $\text{TTS}_{\text{QCBO}}$ .  $\square$

Quantum computers, such as those implementing adiabatic quantum computing (AQC) for solving QUBO problems, face challenges due to limited parameter precision [46]. In theory, QUBO parameters are real-valued, but practical hardware—whether quantum annealers like D-Wave’s or other accelerators—relies on finite precision representations, such as fixed-bit integers [46]. This limitation introduces perturbations in quantum systems, which distort the energy landscape and can shift the global optimum.

Considering directly truncating the Ising coefficients to  $d$  digits, the following lemma shows that the convergence can be preserved under certain conditions.

**Lemma 2** *Let the coefficients of the QUBO problem be truncated to  $d = O(\log n)$  digits. If QCGD is used with these truncated coefficients, it will retain convergence guarantees and the number of iterations remains in the same order.*

The formal proof is presented in the supplementary. This result is appealing because it demonstrates that even with limited precision, the hybrid algorithm can still achieve convergence without a substantial increase in computational effort. This behavior can be interpreted as a form of implicit error correction. The introduced errors are effectively controlled and do not accumulate in a way that disrupts the convergence properties of the algorithm.

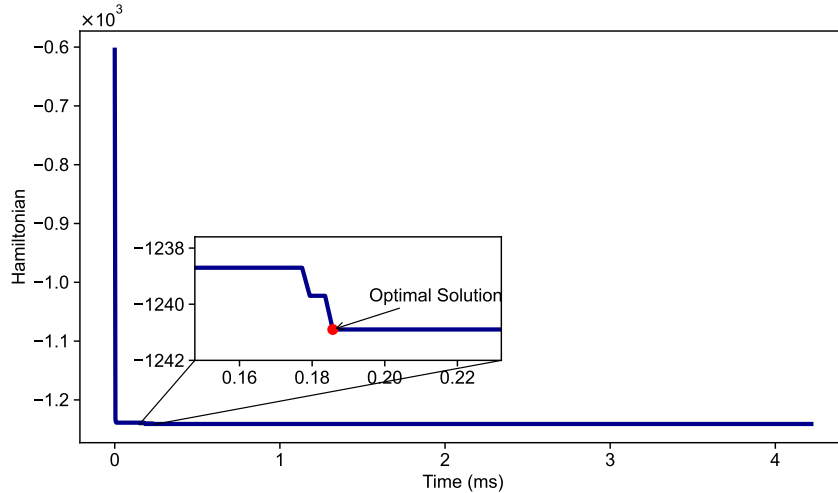
## Experimental validation of quantum advantage

To verify the advantages of the training on neural network, we undertake the experiment using coherent Ising machines for the classification of coat and sandal images from the Fashion MNIST dataset. The dataset consists of 60,000 training images and 10,000 test images, each representing a grayscale clothing item from 10 classes, including T-shirts/tops, trousers, pullovers, dresses, coats, sandals, shirts, sneakers, bags, and ankle boots. Each image is  $28 \times 28$  pixels, with pixel values ranging from 0 to 255. Additional details of the experimental results are deferred to the supplementary.

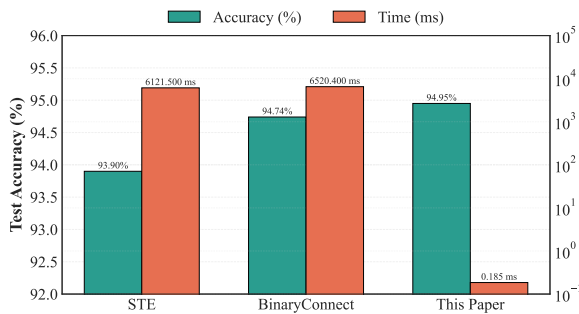
Figure 3a illustrates the energy evolution during the optimization process using CIM to solve the neural network training directly. CIM identifies the optimal solution at the 88th iteration, approaching the optimal value in 0.185 ms, with the resulting model achieving a test accuracy of 94.95%.

To evaluate the performance of our quantum-based approach for training quantized neural networks, we present a series of comparative analyses. Figure 3b compares the test accuracy and running time of our model and quantum approach against previous classical approaches, including straight through estimator (STE) [47] and BinaryConnect [48]. We provide a brief description of the two classical algorithms in the supplementary. Here the proposed quantum-based method achieves a test accuracy of 94.95% with a significantly reduced running time of 0.185 ms, demonstrating superior efficiency and effectiveness.

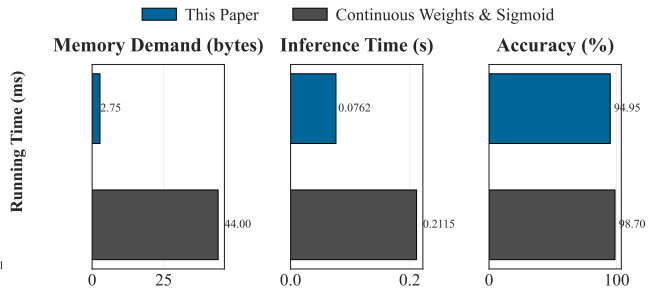
Further, Figure 3c examines the memory demand and inference complexity, contrasting a neural network with continuous weights and sigmoid activation functions against our quantized approach, which approximates the activation function with a simple piecewise linear function. Our method reduces memory cost to 2.75 bytes and inference time to 0.0762 seconds while maintaining a test accuracy of 94.95%, highlighting its resource efficiency. These results collectively underscore the advantages of leveraging quantum computing for training quantized neural networks, offering improvements in speed, and resource efficiency.



(a)



(b)



(c)

Figure 3: (a) Energy evolution curve during the optimization of a quantized neural network using a coherent Ising machine (CIM); (b) Comparative analysis of test accuracy and running time for different training algorithms (STE [47], BinaryConnect [48]); (c) Performance comparison of memory demand, inference time, and accuracy before and after quantization and activation function approximation.

Table 2 summarizes the performance of post-training quantization (PTQ) algorithms under different activation functions and bit widths. As expected, reducing the bit precision generally leads to a degradation in accuracy. While most methods maintain high accuracy at 4-bit and 3-bit precision, a significant drop is

Algorithm	Activation	FP Model	4-bit	3-bit	2-bit
RTN [49]	ReLU	98.7%	95.4%	98.7%	<b>50.0%</b>
	LeakyReLU	98.7%	98.7%	98.7%	<b>75.4%</b>
	Sigmoid	98.7%	97.2%	95.4%	<b>75.4%</b>
AdaRound [9]	ReLU	98.7%	98.7%	98.8%	<b>50.0%</b>
	LeakyReLU	98.7%	98.7%	98.7%	98.7%
	Sigmoid	98.7%	97.2%	95.4%	<b>50.0%</b>
DFQ [50]	ReLU	98.7%	95.4%	98.7%	<b>50.0%</b>
	LeakyReLU	98.7%	98.7%	98.7%	98.7%
	Sigmoid	98.7%	98.7%	98.7%	<b>50.0%</b>

Table 2: Classification accuracy (%) under different PTQ algorithms, activation functions, and bit widths.

observed at 2-bit, especially with ReLU activations. Specifically, our method achieves 94.95% test accuracy with an effective parameter precision of just 1.1 bits, substantially outperforming almost all listed 2-bit baselines. This result highlights the potential of our framework under aggressive quantization.

Spline interpolation requires careful consideration of the number of intervals, as it directly influences qubit resource allocation and must be optimized for quantum hardware constraints. In our experimental setup, we partitioned the input range into four intervals, achieving an optimal trade-off between qubit efficiency and segmentation accuracy. The corresponding breakpoints, defined at  $[-8, -c, 0, c, 8]$ , yielded the following results:

Value of $c$	1	2	3	4	5	6	7
<b>Classification Accuracy</b>	96.35%	98.7%	96.35%	94.95%	96.75%	91.35%	91.35%

Table 3: Accuracy values for different cases of  $c$ .

Note that QUBO problems may yield multiple optimal solutions, and the accuracy shown corresponds to one such solution.

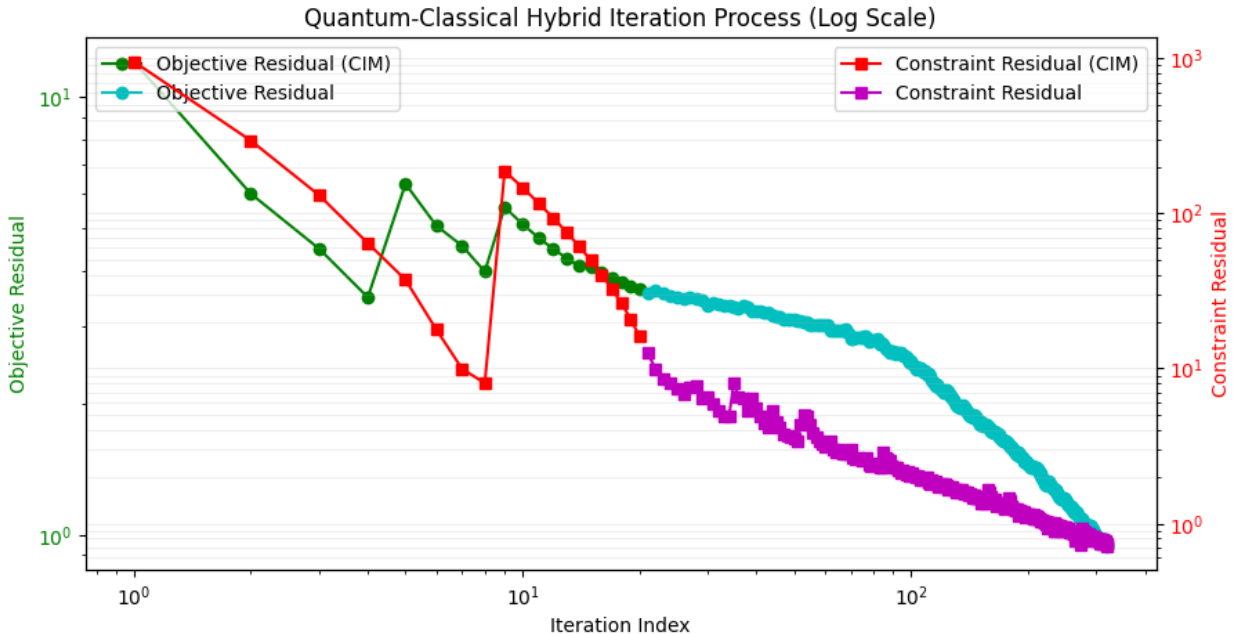


Figure 4: The figure illustrates the convergence of the Quantum Conditional Gradient Descent (QCGD) algorithm using CIM (green and red) and Gurobi (cyan and purple) solvers over 321 iterations on a log-log scale. The left y-axis shows the objective residual, and the right y-axis shows the constraint residual, with lines representing the residuals for CIM (solid) and Gurobi (dashed).

Figure 4 illustrates the convergence behavior of the Quantum Conditional Gradient Descent algorithm when applied to the neural network training utilizing a hybrid quantum-classical approach with CIM and Gurobi solvers. The algorithm achieves convergence to the optimal solution within 321 iterations, with the objective residual and constraint residual presented on a logarithmic scale. The CIM solver exhibits consistent convergence behavior, steadily driving both the objective and constraint residual below the threshold value. In contrast, the Gurobi solver maintains convergence but displays oscillatory patterns in the constraint residual between iterations 30-100. Notably, the hybrid strategy achieves convergence in just 321 iterations, demonstrating its computational efficiency by effectively combining the strengths of CIM and the classical approach. To further validate the robustness and reproducibility of these results, we performed five independent experiments achieving convergence to the optimal solution in 723, 338, 263, 432, and 427 iterations,

respectively. These consistent outcomes across multiple trials confirms its reliability and reproducibility in practical applications.

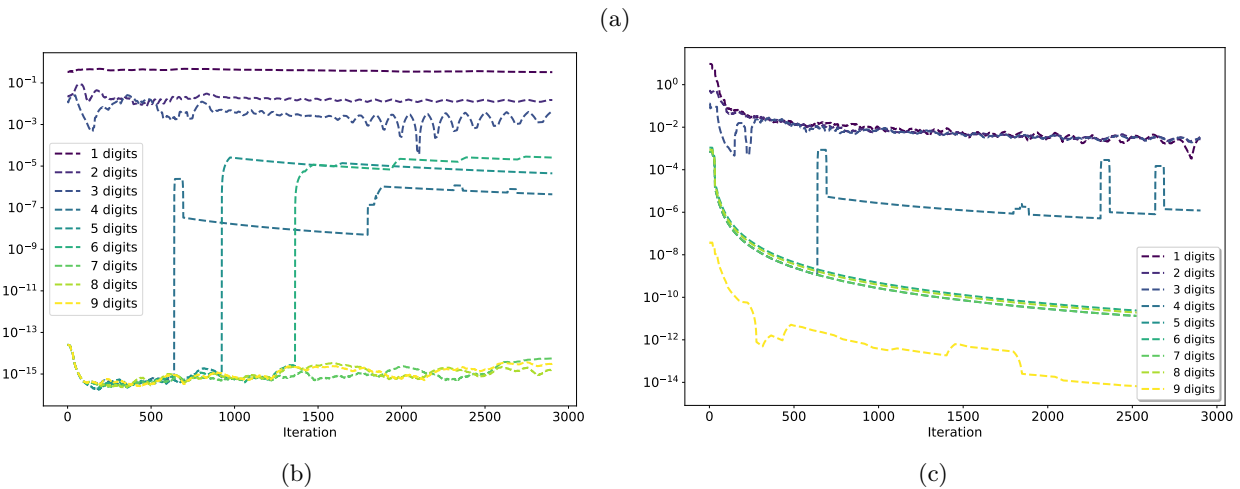
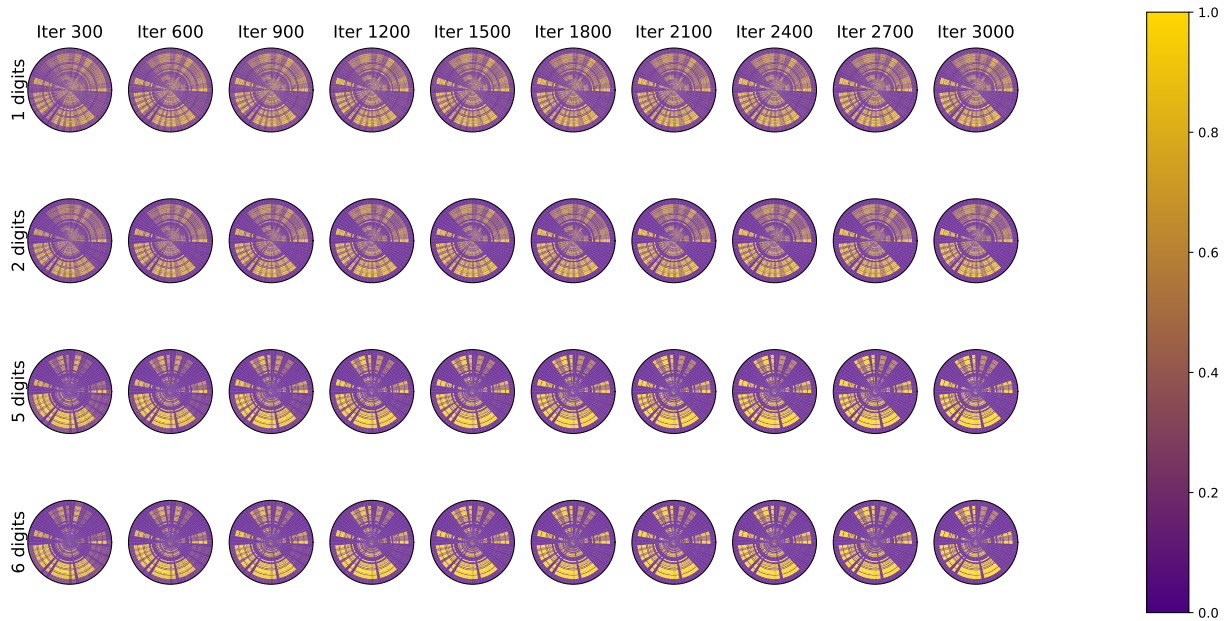


Figure 5: (a) Circular heatmaps depict the evolution of the QUBO matrix during the QCGD algorithm for different significant digit precisions (1 to 6 digits) across selected iterations (300, 600, 900, 1200, 1500, 1800, 2100, 2400, 2700, and 3000). The color intensity represents matrix element values, with the color bar indicating the range from 0.0 (purple) to 1.0 (yellow). Each row corresponds to a specific precision level, illustrating the iterative trajectory and convergence behavior. (b) and (c): The two subplots show the smoothed absolute differences  $|\text{obj}_k - \text{obj}_{10}|$  (left) and  $|\text{residual}_k - \text{residual}_{10}|$  (right) relative to the 10-digit precision baseline across iterations for precision levels of 1 to 9 digits. The y-axis is on a log scale, with dashed lines representing each precision level.

### Robustness of hybrid approach: impact of coefficient matrix rounding

To investigate the convergence behavior of the hybrid algorithm in neural network training under different matrix rounding precision levels, we systematically rounded the matrix coefficients to digit precisions ranging from 1 to 10 decimal places. The algorithm was then executed for each precision setting until convergence to the optimal solution was achieved. Specifically, matrix elements were rounded to 1 through 10 significant

digits, and the corresponding number of iterations required to attain the optimal solution at each precision level was recorded as follows:

These results indicate the variability in convergence speed, with lower precision levels (e.g., 1-3 digits) requiring substantially more iterations (up to 43,343 for 3 digits), likely due to increased numerical instability and larger initial differences. In contrast, higher precision levels (e.g., 5-10 digits) converge more efficiently, with the minimum iterations observed at 2904 for 10 digits, suggesting that increased precision enhances the convergence stability.

Precision (Digits)	1	2	3	4	5	6	7	8	9	10
Iterations to optimal	6303	18130	43343	4746	3993	3787	6099	6643	5871	2904

Table 4: Convergence speed of QCGD algorithm across precision levels

Figure 5a displays the QUBO matrix evolution using circular heatmaps, highlighting the impact of precision levels on iterative trajectories. Despite the differences revealed in these trajectories, our results confirm that all trajectories converge to the optimal solution, consistent with the theoretical convergence of the QCGD algorithm. Notably, even under minimal precision conditions (e.g., 1-digit rounding), matrix adjustments in later iterations remain marginal. These consistently small perturbations across all precision levels suggest that a lazy evaluation strategy for QCGD (Quantum-Constrained Gradient Descent) could be viable. Such an approach would minimize redundant quantum circuit executions, thereby improving computational efficiency on quantum hardware.

The smoothed absolute differences of the objective value and constraint residual relative to the 10-digit precision baseline were recorded, with results visualized in Figure 5b and 5c. This setup allowed us to assess the impact of numerical precision on convergence trajectories. Both subplots demonstrate that differences across all precision levels remain small, typically less than  $10^{-2}$ , indicating the hybrid algorithm’s robustness to precision variations. A downward trend is observed in the difference of constraint residual, with differences decreasing sharply after initial fluctuations and stabilizing post-1500 iterations, confirming convergence to a consistent optimal solution regardless of precision, as supported by prior results. The rapid initial decline in the constraint residual difference, particularly for lower precisions (e.g., 1-3 digits), suggests early sensitivity to numerical accuracy, while the differences remain stably small in later iterations. The near-overlap of higher precision curves (e.g., 7-9 digits) highlights diminishing returns from increased precision.

## Methods

### Copositive Programming Framework

The QCGD method is build on copositive programming (CP) [51] which is a mathematical optimization branch that has garnered significant attention for its applications in various optimization problems. In copositive programming, the objective is to optimize over the cone of copositive matrices, which are matrices for which the quadratic form yields nonnegative values over the nonnegative orthant. One key application of copositive programming is in transforming binary quadratic problems into completely positive problems. This transformation involves reformulating the standard quadratic problem as a CP program, enabling the optimization of a quadratic form over the Cartesian product of simplices.

Consider the following linear constrained quadratic binary programming problem,

$$\min \mathbf{x}^T \mathbf{Q} \mathbf{x} \tag{33}$$

$$s.t. \mathbf{A} \mathbf{x} = \mathbf{b}. \tag{34}$$

According to [45, 51], the quadratic objective and linear constraints of the quadratic binary optimization problem can be represented as linear functions of a copositive matrix, and the problems (33)-(34) can be converted to the completely positive program.

In practice, we often encounter constraints in quadratic binary programming problems that are not only linear but may also be quadratic or even of higher order. For example, in the inequality (11) of the

previous model, quadratic terms appear, requiring us to reduce the order of the problem. Recognizing that the copositive programming (CP) framework is suitable for handling constrained problems and can tolerate additional constraints, we can perform variable transformations and add extra constraints to reduce the order of the problem.

Consider the following quadratic 0-1 programming problem with quadratic constraints programming,

$$\min \mathbf{x}^T \mathbf{Q}_0 \mathbf{x} \quad (35)$$

$$s.t. \mathbf{A} \mathbf{x} = \mathbf{b} \quad (36)$$

$$\mathbf{x}^T \mathbf{Q}_t \mathbf{x} \leq c_t, 1 \leq t \leq T \quad (37)$$

To linearize the quadratic constraint, we can use  $x_{ij} \in \{0, 1\}$  to represent the product of  $x_i$  and  $x_j$ , by adding the following constraints:  $x_{ij} \leq x_i, x_{ij} \leq x_j, x_{ij} \geq x_i + x_j - 1$ . It can be seen that  $x_{ij} = x_i \cdot x_j$  always holds under these constraints.

In addition, we have the following improved linearization procedure. Consider the term  $z_{x,j,k}^l = w_{jk}^l a_{x,k}^{l-1}$  in QCBO model, which can be expressed as  $z_{x,j,k}^l = \sum_{\ell=1}^{\bar{\ell}} 2^\ell \cdot w_{jk}^l \cdot \delta_{a_{x,k}^l}^{(\ell)}$ . In our neural network training model, quadratic constraints arise from the  $w_{jk}^l a_{x,k}^{l-1}$  terms. Note that the bilinear components involving  $w_{jk}^l$  and  $a_{x,k}^{l-1}$  share the common variable  $w_{jk}^l$ . To linearize these terms effectively, we can use the following constraints:

$$\sum_{\ell=1}^{\bar{\ell}} 2^\ell \cdot \delta_{a_{x,k}^l}^{(\ell)} + (2^{\bar{\ell}+1} - 2) \cdot w_{jk}^l - z_{x,j,k}^l \leq 2^{\bar{\ell}+1} - 2, \quad (38)$$

$$z_{x,j,k}^l \leq \sum_{\ell=1}^{\bar{\ell}} 2^\ell \cdot \delta_{a_{x,k}^l}^{(\ell)}, \quad (39)$$

$$z_{x,j,k}^l \leq (2^{\bar{\ell}+1} - 2) \cdot w_{jk}^l. \quad (40)$$

Note that here we treat  $w_{jk}^\ell$  as binary variables; for integer-valued  $w_{jk}^\ell$ , the linearization process described above is still applicable. We only need to perform the same operation on the bits of the binary encoding of  $w_{jk}^\ell$  and  $a_{x,k}^{l-1}$ .

## Quantum-Conditional Gradient Descent and Lazy Implementation

QCGD algorithm runs for  $T$  iterations, with the following steps at each iteration  $t$ :

1. Set the step size  $\gamma_t = 2/(\delta(t+1))$  and penalty parameter  $\alpha_t = \alpha_0 \sqrt{\delta t + 1}$ , where  $\delta > 0$  is a scaling factor and  $\alpha_0 = 1$  by default.
2. Compute errors in satisfying equality constraints ( $\mathbf{g}_t$ ) and inequality constraints ( $\mathbf{g}'_t$ ) based on the current solution matrix  $\mathbf{V}_t$ .
3. Form the gradient matrix  $\mathbf{G}_t$  using the coefficient matrix in the copositive programming formulation and constraint errors above. To ensure convergence, solve the subproblem  $\min_{\mathbf{w} \in \mathbb{Z}_2^p} \mathbf{w}^\top \mathbf{G}_t \mathbf{w}$   $m_t$  times on a quantum annealer, selecting the best solution as:

$$\mathbf{w}_t = \arg \min_{\mathbf{w}^{(k)}, k=1, \dots, m_t} \left\{ \mathbf{w}^{(k)\top} \mathbf{G}_t \mathbf{w}^{(k)} \right\}, \quad (41)$$

where  $\mathbf{w}^{(k)}$  is the  $k$ -th solution. Set the update direction as  $\mathbf{H}_t = \mathbf{w}_t \mathbf{w}_t^\top$ .

4. Update the solution:  $\mathbf{V}_{t+1} = (1 - \eta_t) \mathbf{V}_t + \eta_t \mathbf{H}_t$ .
5. Update the dual variables  $\mathbf{z}_t$  and  $\mathbf{z}'_t$  using the step size  $\gamma$ .
6. After  $T$  iterations, extract a binary solution  $\mathbf{x}$  from  $\mathbf{V}$ , either directly from its first column or by computing the top singular vector of a submatrix and projecting onto the feasible set (e.g., using the Hungarian algorithm for permutation constraints).

The practical implementation of the QCGD algorithm is challenged by the error rates associated with quantum computers, leading to inaccuracies in the computation results. This inaccuracy is particularly pronounced in the oracle, which plays a crucial role in the QCGD algorithm by providing direction in each iteration. The consideration of the *inexact oracle* in the context of QCGD is therefore crucial for several reasons. Firstly, due to the inherent limitations of quantum hardware, achieving perfect precision in quantum computations is challenging. The inexactness in the oracle reflects these limitations and underscores the need to develop algorithms that are robust to such imperfections. Secondly, the use of an inexact oracle also introduces a trade-off between computational accuracy and efficiency.

**Definition 1** ( $(\delta, \varepsilon)$ -Inexact oracle [52, 53]) *For problem*

$$\min_{\mathbf{D}} \text{Tr}(\mathbf{Q}_{\text{QUBO}}^{(t)} \mathbf{D}) \quad (42)$$

*over the cone of completely positive matrices, if  $\mathbf{D}_t$  obtained from the oracle satisfies the following condition:*

$$\text{Tr}(\mathbf{Q}_{\text{QUBO}}^{(t)} (\mathbf{D}_t - \mathbf{V}_t)) \leq \delta \cdot \text{Tr}(\mathbf{Q}_{\text{QUBO}}^{(t)} (\mathbf{D}_t^* - \mathbf{V}_t)) + \frac{\xi_t}{\sqrt{t}}, \quad (43)$$

*where  $\mathbf{D}_t^*$  is the exact optimal solution,  $\delta \in (0, 1]$  denotes relative error bound,  $\xi_t$  represents the random additive error with  $\mathbb{E}[\xi_t] \leq \varepsilon$ . Then  $\mathbf{D}_t$  is said to be an output of a  $(\delta, \varepsilon)$ -Inexact oracle.*

A quantum computer without any imperfections corresponds to the scenario where  $\delta = 1$  and  $\varepsilon = 0$ . The following lemma indicates that convergence can still be achieved even if the single quantum computation acts as an inexact oracle. This theoretical framework ensures that the overall algorithm remains robust despite potential inaccuracies in the quantum computation. Theoretical proof follows from that in [45], and we include it in the supplementary for completeness.

**Proposition 1** *Under  $(\delta, \varepsilon)$ -Inexact oracle, the objective gap and infeasibility in the  $T$ -th iteration of the hybrid algorithm satisfies that*

$$\mathbb{E}[\text{Objective-gap}_T] = O\left(\frac{(1 + \varepsilon)}{\sqrt{\delta^{3/2} T}}\right), \mathbb{E}[\text{Infeasibility}_T] = O\left(\frac{(1 + \varepsilon)}{\sqrt{\delta^{3/2} T}}\right) \quad (44)$$

*Here  $\text{Objective-gap}_T$  denotes the objective value of the solution obtained at the  $T$ -th iteration and the optimal objective value;  $\text{Infeasibility}_T$  represents the distance from the solution obtained at the  $T$ -th iteration to the feasible region. In addition, the bound in (44) holds with probability at least  $1 - \frac{\max \text{Var}[\xi_s]}{\varepsilon^2 T}$ .*

To reduce unnecessary computation, we can adopt a lazy implementation strategy, where solving the QUBO problem is applied only when significant changes occur. This approach is motivated by the observation that, in later iterations, the magnitude of QUBO coefficient modifications often becomes negligible. We can determine whether solving the QUBO problem is necessary based on the *spectral gap*:

$$\Delta_t = \min_{\mathbf{D} \neq \mathbf{D}_t^*} \text{Tr}(\mathbf{Q}_{\text{QUBO}}^{(t)} \mathbf{D}) - \min_{\mathbf{D}} \text{Tr}(\mathbf{Q}_{\text{QUBO}}^{(t)} \mathbf{D}) \quad (45)$$

which is defined as the difference between the lowest and the second-lowest objective value of the QUBO problem. If the cumulative changes in the coefficients of the QUBO matrix fall below a certain threshold, *i.e.*,

$$\|\mathbf{Q}_{\text{QUBO}}^{(t+1)} - \mathbf{Q}_{\text{QUBO}}^{(t)}\|_F < \Delta_t, \quad (46)$$

Then, it implies that the perturbations in the solution landscape are insignificant. Consequently, the algorithm can bypass solving the latest QUBO problem. By leveraging this stability, potentially through a threshold-based criterion to detect negligible changes, computational overhead can be reduced, particularly in resource-constrained environments.

## Conclusion

In conclusion, this paper introduces a QUBO-based framework that enables arbitrary activation and loss functions through spline interpolation, significantly expanding the applicability of quantum computing in neural network training. The theoretically derived upper bound on Ising spin requirements, along with the empirically validated convergence of our hybrid algorithm, even under randomized outputs and limited coefficient matrix precision, further validates the robustness of our approach. The comparison with classical methods highlights the superior performance of the Ising machine in quantized neural network training, while the hybrid algorithm demonstrates consistent efficacy and stability. Meanwhile, our model offers promising potential for applications demanding trainable activation functions, paving the way for quantum-enhanced neural architectures. This work represents a pivotal advancement toward harnessing the full potential of quantum-accelerated machine learning in real-world implementations.

## References

- [1] Devlin, J., Chang, M.-W., Lee, K. & Toutanova, K. Bert: Pre-training of deep bidirectional transformers for language understanding. In *Proceedings of the 2019 conference of the North American chapter of the association for computational linguistics: human language technologies, volume 1 (long and short papers)*, 4171–4186 (2019).
- [2] Dosovitskiy, A. *et al.* An image is worth 16x16 words: Transformers for image recognition at scale. In *9th International Conference on Learning Representations, ICLR 2021*.
- [3] Chen, W. *et al.* Early detection of visual impairment in young children using a smartphone-based deep learning system. *Nature medicine* **29**, 493–503 (2023).
- [4] Almalioglu, Y., Turan, M., Trigoni, N. & Markham, A. Deep learning-based robust positioning for all-weather autonomous driving. *Nature machine intelligence* **4**, 749–760 (2022).
- [5] Liu, H.-I. *et al.* Lightweight deep learning for resource-constrained environments: A survey. *ACM Computing Surveys* **56**, 1–42 (2024).
- [6] Hubara, I., Courbariaux, M., Soudry, D., El-Yaniv, R. & Bengio, Y. Quantized neural networks: Training neural networks with low precision weights and activations. *Journal of Machine Learning Research* **18**, 1–30 (2018).
- [7] Ignatov, A. *et al.* Ai benchmark: Running deep neural networks on android smartphones. In *Proceedings of the European Conference on Computer Vision (ECCV) Workshops*, 0–0 (2018).
- [8] Jacob, B. *et al.* Quantization and training of neural networks for efficient integer-arithmetic-only inference. In *Proceedings of the IEEE conference on computer vision and pattern recognition*, 2704–2713 (2018).
- [9] Nagel, M., Amjad, R. A., Van Baalen, M., Louizos, C. & Blankevoort, T. Up or down? adaptive rounding for post-training quantization. In *International conference on machine learning*, 7197–7206 (PMLR, 2020).
- [10] Liu, Z., Cheng, K.-T., Huang, D., Xing, E. P. & Shen, Z. Nonuniform-to-uniform quantization: Towards accurate quantization via generalized straight-through estimation. In *Proceedings of the IEEE/CVF conference on computer vision and pattern recognition*, 4942–4952 (2022).
- [11] Wang, Z., Marandi, A., Wen, K., Byer, R. L. & Yamamoto, Y. Coherent ising machine based on degenerate optical parametric oscillators. *Physical Review A* **88**, 063853 (2013).
- [12] Inagaki, T. *et al.* A coherent ising machine for 2000-node optimization problems. *Science* **354**, 603–606 (2016).
- [13] Honjo, T. *et al.* 100,000-spin coherent ising machine. *Science advances* **7**, eabh0952 (2021).

- [14] Mohseni, N., McMahon, P. L. & Byrnes, T. Ising machines as hardware solvers of combinatorial optimization problems. *Nature Reviews Physics* **4**, 363–379 (2022).
- [15] Kleyko, D. *et al.* Efficient optimization with higher-order ising machines. *Nature Communications* **14** (2023).
- [16] Yue, W. *et al.* A scalable universal ising machine based on interaction-centric storage and compute-in-memory. *Nature Electronics* **7**, 904–913 (2024).
- [17] Takesue, H. *et al.* Finding independent sets in large-scale graphs with a coherent ising machine. *Science Advances* **11**, eads7223 (2025).
- [18] Böhm, F., Alonso-Urquijo, D., Verschaffelt, G. & Van der Sande, G. Noise-injected analog ising machines enable ultrafast statistical sampling and machine learning. *Nature Communications* **13**, 5847 (2022).
- [19] Yamashita, H. *et al.* Low-rank combinatorial optimization and statistical learning by spatial photonic ising machine. *Physical Review Letters* **131**, 063801 (2023).
- [20] Laydevant, J., Marković, D. & Grollier, J. Training an ising machine with equilibrium propagation. *Nature Communications* **15**, 3671 (2024).
- [21] Niazi, S. *et al.* Training deep boltzmann networks with sparse ising machines. *Nature Electronics* **7**, 610–619 (2024).
- [22] Kim, M., Venturelli, D. & Jamieson, K. Leveraging quantum annealing for large mimo processing in centralized radio access networks. In *Proceedings of the ACM special interest group on data communication (SIGCOMM)*, 241–255 (2019).
- [23] Li, W. *et al.* Unified sparse optimization via quantum architectures and hybrid techniques. *Quantum Science and Technology* **10**, 025059 (2025).
- [24] Zha, J. *et al.* Encoding molecular docking for quantum computers. *Journal of Chemical Theory and Computation* **19**, 9018–9024 (2023).
- [25] Li, J. & Ghosh, S. Quantum-soft qubo suppression for accurate object detection. In *European Conference on Computer Vision (ECCV)*, 158–173 (2020).
- [26] Birdal, T., Golyanik, V., Theobalt, C. & Guibas, L. J. Quantum permutation synchronization. In *Proceedings of the IEEE/CVF Conference on Computer Vision and Pattern Recognition (CVPR)*, 13122–13133 (2021).
- [27] Benkner, M. S. *et al.* Q-match: Iterative shape matching via quantum annealing. In *Proceedings of the IEEE/CVF International Conference on Computer Vision (ICCV)*, 7586–7596 (2021).
- [28] Zaech, J.-N., Liniger, A., Danelljan, M., Dai, D. & Van Gool, L. Adiabatic quantum computing for multi object tracking. In *Proceedings of the IEEE/CVF Conference on Computer Vision and Pattern Recognition (CVPR)*, 8811–8822 (2022).
- [29] Arrigoni, F., Menapace, W., Benkner, M. S., Ricci, E. & Golyanik, V. Quantum motion segmentation. In *European Conference on Computer Vision (ECCV)*, 506–523 (2022).
- [30] Bhatia, H. *et al.* Ccuantumm: Cycle-consistent quantum-hybrid matching of multiple shapes. In *Proceedings of the IEEE/CVF Conference on Computer Vision and Pattern Recognition (CVPR)*, 1296–1305 (2023).
- [31] Apicella, A., Donnarumma, F., Isgro, F. & Prevete, R. A survey on modern trainable activation functions. *Neural Networks* **138**, 14–32 (2021).
- [32] Abel, S., Criado, J. C. & Spannowsky, M. Completely quantum neural networks. *Physical Review A* **106**, 022601 (2022).

- [33] Leshno, M., Lin, V. Y., Pinkus, A. & Schocken, S. Multilayer feedforward networks with a nonpolynomial activation function can approximate any function. *Neural networks* **6**, 861–867 (1993).
- [34] Hornik, K. Approximation capabilities of multilayer feedforward networks. *Neural networks* **4**, 251–257 (1991).
- [35] Lucas, A. Ising formulations of many np problems. *Frontiers in physics* **2**, 5 (2014).
- [36] Pelofske, E. Comparing three generations of d-wave quantum annealers for minor embedded combinatorial optimization problems. *Quantum Science and Technology* (2023).
- [37] Mirkarimi, P., Shukla, I., Hoyle, D. C., Williams, R. & Chancellor, N. Quantum optimization with linear ising penalty functions for customer data science. *Physical Review Research* **6**, 043241 (2024).
- [38] Ding, Y., Liu, J., Xiong, J. & Shi, Y. On the universal approximability and complexity bounds of quantized relu neural networks. In *2019 International Conference on Learning Representations*.
- [39] Yarotsky, D. Error bounds for approximations with deep relu networks. *Neural networks* **94**, 103–114 (2017).
- [40] Miyato, T., Kataoka, T., Koyama, M. & Yoshida, Y. Spectral normalization for generative adversarial networks. In *International Conference on Learning Representations* (2018).
- [41] Rosenberg, I. G. Reduction of bivalent maximization to the quadratic case. (1975).
- [42] Bartlett, P. L., Harvey, N., Liaw, C. & Mehrabian, A. Nearly-tight vc-dimension and pseudodimension bounds for piecewise linear neural networks. *Journal of Machine Learning Research* **20**, 1–17 (2019).
- [43] Cover, T. M. Capacity problems for linear machines. *Pattern recognition* 283–289 (1968).
- [44] Shalev-Shwartz, S. & Ben-David, S. *Understanding machine learning: From theory to algorithms* (Cambridge university press, 2014).
- [45] Yurtsever, A., Birdal, T. & Golyanik, V. Q-fw: A hybrid classical-quantum frank-wolfe for quadratic binary optimization. In *European Conference on Computer Vision (ECCV)*, 352–369 (2022).
- [46] Mücke, S., Gerlach, T. & Piatkowski, N. Optimum-preserving qubo parameter compression. *Quantum Machine Intelligence* **7**, 1–18 (2025).
- [47] Bengio, Y., Léonard, N. & Courville, A. Estimating or propagating gradients through stochastic neurons for conditional computation. *arXiv preprint arXiv:1308.3432* .
- [48] Courbariaux, M., Bengio, Y. & David, J.-P. Binaryconnect: Training deep neural networks with binary weights during propagations. *Advances in neural information processing systems* (2015).
- [49] Kogan, A. Is (selective) round-to-nearest quantization all you need? *arXiv preprint arXiv:2505.15909* (2025).
- [50] Nagel, M., Baalen, M. v., Blankevoort, T. & Welling, M. Data-free quantization through weight equalization and bias correction. In *Proceedings of the IEEE/CVF international conference on computer vision*, 1325–1334 (2019).
- [51] Burer, S. On the copositive representation of binary and continuous nonconvex quadratic programs. *Mathematical Programming* **120**, 479–495 (2009).
- [52] Dunn, J. C. & Harshbarger, S. Conditional gradient algorithms with open loop step size rules. *Journal of Mathematical Analysis and Applications* **62**, 432–444 (1978).
- [53] Locatello, F., Khanna, R., Tschannen, M. & Jaggi, M. A unified optimization view on generalized matching pursuit and frank-wolfe. In *Artificial intelligence and statistics*, 860–868 (2017).
- [54] Song, X. *et al.* Training multi-layer neural networks on ising machine. *arXiv:2311.03408* (2023).
- [55] Nagel, M. *et al.* A white paper on neural network quantization. *arXiv preprint arXiv:2106.08295* .

## Supplementary Material

### A Error Bound of Piecewise Linear Approximation in FNN

**Proof:** Define layer-wise activations:

$$h_0 = x, \quad h_l = \sigma(\mathbf{W}_l h_{l-1} + \mathbf{b}_l), \quad \hat{h}_0 = x, \quad \hat{h}_l = \hat{\sigma}(\mathbf{W}_l \hat{h}_{l-1} + \mathbf{b}_l), \quad l = 1, \dots, L-1. \quad (47)$$

The output error is:

$$\|f(x) - \hat{f}(x)\|_2 = \|\mathbf{W}_L(h_{L-1} - \hat{h}_{L-1})\|_2 \leq \|h_{L-1} - \hat{h}_{L-1}\|_2, \quad (48)$$

since  $\|\mathbf{W}_L\|_2 \leq 1$ . Let  $\delta_l = \|h_l - \hat{h}_l\|_2$ . We bound  $\delta_l$  recursively.

For layer  $l$ , consider:

$$h_l - \hat{h}_l = \sigma(\mathbf{W}_l h_{l-1} + \mathbf{b}_l) - \hat{\sigma}(\mathbf{W}_l \hat{h}_{l-1} + \mathbf{b}_l). \quad (49)$$

Decompose as:

$$h_l - \hat{h}_l = \left[ \sigma(\mathbf{W}_l h_{l-1} + \mathbf{b}_l) - \sigma(\mathbf{W}_l \hat{h}_{l-1} + \mathbf{b}_l) \right] + \left[ \sigma(\mathbf{W}_l \hat{h}_{l-1} + \mathbf{b}_l) - \hat{\sigma}(\mathbf{W}_l \hat{h}_{l-1} + \mathbf{b}_l) \right]. \quad (50)$$

The first term, using  $L_\sigma \leq 1$ , is:

$$\|\sigma(\mathbf{W}_l h_{l-1} + \mathbf{b}_l) - \sigma(\mathbf{W}_l \hat{h}_{l-1} + \mathbf{b}_l)\|_2 \leq L_\sigma \|\mathbf{W}_l h_{l-1} - \mathbf{W}_l \hat{h}_{l-1}\|_2 \leq \|\mathbf{W}_l\|_2 \delta_{l-1} \leq \delta_{l-1}. \quad (51)$$

The second term, by the approximation error, satisfies:

$$\|\sigma(\mathbf{W}_l \hat{h}_{l-1} + \mathbf{b}_l) - \hat{\sigma}(\mathbf{W}_l \hat{h}_{l-1} + \mathbf{b}_l)\|_2 = \sqrt{\sum_{i=1}^{m_l} |\sigma(z_i) - \hat{\sigma}(z_i)|^2} \leq \sqrt{m_l} \epsilon_\sigma \leq \sqrt{m} \epsilon_\sigma, \quad (52)$$

where  $z = \mathbf{W}_l \hat{h}_{l-1} + \mathbf{b}_l$ . Thus:

$$\delta_l \leq \delta_{l-1} + \sqrt{m} \epsilon_\sigma. \quad (53)$$

Solving the recursion, we can obtain that  $\delta_l \leq l\sqrt{m}\epsilon_\sigma$ . For the output:

$$\|f(x) - \hat{f}(x)\|_2 \leq \delta_{L-1} \leq (L-1)\sqrt{m}\epsilon_\sigma \leq L\sqrt{m}\epsilon_\sigma. \quad (54)$$

To determine  $n$ , assume  $\sigma$  has  $\|\sigma''\|_\infty \leq M$ . Construct  $\hat{\sigma}$  over  $[-R, R]$  with  $n$  equal segments, each of width  $h = \frac{2R}{n}$ . The interpolation error is:

$$|\sigma(z) - \hat{\sigma}(z)| \leq \frac{1}{8} h^2 \|\sigma''\|_\infty = \frac{1}{8} \left(\frac{2R}{n}\right)^2 M = \frac{R^2 M}{2n^2}. \quad (55)$$

Set  $\frac{R^2 M}{2n^2} \leq \epsilon$ , we have

$$n \geq \sqrt{\frac{R^2 M}{2\epsilon}}, \quad n = O\left(\frac{1}{\sqrt{\epsilon}}\right). \quad (56)$$

□

### B Spline Quantumization Protocol

Quantum computing faces the formidable challenge of not only optimizing QUBO models but also addressing highly nonlinear optimization problems as optimization targets. The significance of this issue lies in its ubiquity across diverse scientific and industrial domains, where real-world problems often exhibit intricate,

arbitrary relationships among variables. This fact underscores the urgency for quantum algorithms capable of navigating and optimizing complex, highly nonlinear landscapes.

Formally we consider the following problem:

$$\min_{\mathbf{x} \in \{0,1\}^n} f(h(\mathbf{x})), \quad (57)$$

where  $f(\cdot)$  is a function of arbitrary form. This formal definition of the optimization problem unlocks the further potential of quantum computing in solving real-world optimization problems. A powerful approach to approximate highly nonlinear functions is to use spline interpolation. Splines are piecewise linear functions that provide a smooth and flexible fit to data points. Spline interpolation can transform the optimization landscape into a more tractable form, making it amenable to quantum optimization algorithms. The spline fitting process involves the following steps:

- **Knot Selection.** Choose a set of knots  $\{M_i\}_{i=1}^n$  which are the points in the domain of  $f(\cdot)$  where the piecewise polynomial segments will join. These knots should be chosen to adequately capture the variability of  $f(\cdot)$  over the entire domain, as the placement of knots can significantly affect the accuracy of the spline approximation.
- **Spline Construction.** Define linear functions  $S_i(x)$  for each segment between consecutive knots.
- **Spline Approximation.** Replace the original function  $f(\cdot)$  with the spline function  $S(\cdot)$ . The spline function can be expressed as:

$$S(h(\mathbf{x})) = \sum_{i=1}^n S_i(h(\mathbf{x})) \cdot \beta_i, \quad (58)$$

where  $\beta_i \in \{0, 1\}$  denotes whether  $h(\mathbf{x})$  is in the  $i$ -th interval.

## B.1 Piecewise Constant Segment

An effective method for simplifying highly nonlinear functions is piecewise constant fitting. This approach approximates the function  $f(\cdot)$  using constant segments, which can reduce the complexity of the optimization problem and facilitate the translation into a QUBO model.

$$\min \sum_{i=0}^n \beta_i \cdot S(M_i) \quad (59)$$

$$s.t. \sum_{i=1}^n \beta_i \cdot M_{i-1} \leq h(\mathbf{x}) \leq \sum_{i=1}^n \beta_i \cdot M_i \quad (60)$$

$$\sum_{i=1}^n \beta_i = 1, \beta_i \in \{0, 1\} \quad (61)$$

**Dealing with the inequality constraint.** We have now derived a QUBO model capable of approximately solving optimization problems with arbitrary objective functions in (B). However, it is important to note that in representing  $\beta_i$ , we introduced two inequality constraints. Here, we introduce the following two approaches:

- Adding a penalty term  $(\sum_{i=1}^n \beta_i M_{i-1} + s - h(\mathbf{x}))^2$ , where  $s \in [0, \Delta M]$ , assuming all the intervals are of length  $\Delta M$ .
- For  $s \in [-\frac{1}{2}, \frac{1}{2}]$ , adding a penalty term

$$\sum_{i=1}^{n-1} \beta_i \cdot \left( \frac{2h(\mathbf{x}) - (M_{i-1} + M_i)}{2(M_i - M_{i-1})} + s \right)^2 + \left( 1 - \sum_{i=1}^{n-1} \beta_i \right) \left( \frac{2h(\mathbf{x}) - (M_{n-1} + M_n)}{2(M_n - M_{n-1})} + s \right)^2. \quad (62)$$

It is important to note that the higher order terms cancel out when the expression is expanded.

We have the following theorem that elucidates the correctness of the second approach.

**Theorem 4** *Let  $\beta^*$  be the optimal solution vector for the following optimization problem,*

$$\min_{\beta} \left\{ \sum_{i=1}^n \beta_i \cdot \left( \frac{2h(\mathbf{x}) - (M_{i-1} + M_i)}{2(M_i - M_{i-1})} \right)^2 \mid \sum_{i=1}^n \beta_i = 1 \right\}. \quad (63)$$

*Then  $\beta_i^* = 1$  only at index  $i = i_{\mathbf{x}}$ , where  $M_{i_{\mathbf{x}}-1} \leq h(\mathbf{x}) \leq M_{i_{\mathbf{x}}}$ , while all other  $\beta_i^*$  are equal to 0.*

**Proof:** To establish this conclusion, it suffices to observe the following: For  $i = i_{\mathbf{x}}$ ,  $|2h(\mathbf{x}) - (M_{i_{\mathbf{x}}-1} + M_{i_{\mathbf{x}}})| \leq M_{i_{\mathbf{x}}} - M_{i_{\mathbf{x}}-1}$  and hence  $\left(\frac{2h(\mathbf{x}) - (M_{i_{\mathbf{x}}-1} + M_{i_{\mathbf{x}}})}{2(M_{i_{\mathbf{x}}} - M_{i_{\mathbf{x}}-1})}\right)^2 \leq \frac{1}{4}$ . And for  $i \neq i_{\mathbf{x}}$ , we have  $\left(\frac{2h(\mathbf{x}) - (M_{i-1} + M_i)}{2(M_i - M_{i-1})}\right)^2 > \frac{1}{4}$ .  $\square$

Theorem 4 establishes that the penalty term in the new model effectively guides the values of  $\beta_i$  to accurately represent the interval in which  $h(\mathbf{x})$  resides. In fact, this new penalty term represents the squared weighted sum of distances from  $h(\mathbf{x})$  to the midpoints of each interval. Consequently, the minimization of this penalty term incentivizes  $\beta_i$  to take values that precisely indicate the correct interval for  $h(\mathbf{x})$ .

Building upon the versatility of spline approximation in simplifying complex optimization landscapes, we use the following sign function as an example to illustrate the efficiency of our approach.

**Example 1 (Sign function)** *sign(x) (1 if  $x \geq 0$  else  $-1$ ) can be represented as*

$$\text{sign}(x) = \min_{\beta \in \{0,1\}} \left\{ (2\beta - 1) + \lambda \cdot \left[ \beta \cdot \left( \frac{2x - M}{2M} + s \right)^2 + (1 - \beta) \cdot \left( \frac{2x + M}{2M} + s \right)^2 \right] \right\}, \quad (64)$$

*where  $M = \sup |x|$  and  $s \in [-\frac{1}{2}, \frac{1}{2}]$  is a slack variable.*

Compared with the model in [54], we do not need to introduce the intermediate variable. Additionally, when representing the sign activation function, we do not need to introduce auxiliary variables for order reduction, as done in [54]. These optimizations can save  $O(WDN \log W)$  bits for us, where  $W, D, N$  denote the network width, network depth and dataset size respectively. Indeed we are able to reduce the coefficients of the highest-order terms in the model's qubit count by 50%.

## C Proof of Convergence of QCGD with Random Quantum Oracle

**Proof:** Similar as [45], the algorithm utilizes an augmented Lagrangian function, defined as

$$\mathcal{Q}_{\alpha}(\mathbf{V}, \mathbf{z}) = \text{Tr}(\mathbf{C}\mathbf{V}) + \mathbf{z}^{\top}(\mathcal{L}\mathbf{V} - \mathbf{v}) + \frac{\alpha}{2} \|\mathcal{L}\mathbf{V} - \mathbf{v}\|^2 \quad \text{for } \mathbf{V} \in \Delta^p, \quad (65)$$

where  $\mathbf{V}$  represents the primal variable,  $\mathbf{z}$  is the dual variable,  $\alpha$  is the penalty parameter,  $\mathbf{C}$  is the cost matrix,  $\mathcal{L}$  denotes the matrix for linear constraints, and  $\mathbf{v}$  is the vector of constraint values.

The QCGD algorithm begins by initializing  $\alpha$ ,  $\mathbf{V}$  and  $\mathbf{z}$ , and then iterates through primal and dual updates. In the primal step, the algorithm computes the gradient of the augmented Lagrangian with respect to  $\mathbf{V}$  and finds a direction that minimizes the linearized loss. This step involves solving a standard QUBO problem to determine the update direction. The primal variable  $\mathbf{V}$  is then updated by taking a step towards this direction. In the dual step, the gradient of the augmented Lagrangian with respect to  $\mathbf{z}$  is computed, and  $\mathbf{z}$  is updated using gradient ascent. Over iterations, the penalty parameter  $\alpha$  is increased as  $\alpha_i = \alpha_0 \sqrt{\delta i + 1}$  to ensure that  $\mathbf{V}$  converges to a feasible solution that satisfies the constraints.

We can obtain the following inequalities:

- The smoothness of  $\mathcal{Q}_{\alpha_t}$ :

$$\mathcal{Q}_{\alpha_t}(\mathbf{V}_{t+1}, \mathbf{z}_t) \leq \mathcal{Q}_{\alpha_t}(\mathbf{V}_t, \mathbf{z}_t) + \gamma_t \cdot \delta \cdot \text{Tr}(\mathbf{Q}_{\text{QUBO}}^{(t)}(\mathbf{V}_{\star} - \mathbf{V}_t)) + O\left(\alpha_t \gamma_t^2 + \frac{\xi_t \gamma_t}{\sqrt{t}}\right). \quad (66)$$

- Definition of  $\mathbf{Q}_{\text{QUBO}}^{(t)}$ :

$$\gamma_t \cdot \delta \cdot \text{Tr}(\mathbf{Q}_{\text{QUBO}}^{(t)}(\mathbf{V}_{\star} - \mathbf{V}_t)) \leq \gamma_t \cdot \delta \cdot \text{Tr}(\mathbf{C}\mathbf{V}_{\star}) - \gamma_t \cdot \delta \cdot \mathcal{Q}_{\alpha_t}(\mathbf{V}_t, \mathbf{z}_t) - \gamma_t \cdot \delta \cdot \frac{\alpha_t}{2} \|\mathcal{L}\mathbf{V}_t - \mathbf{v}\|^2. \quad (67)$$

Combining (66) and (67), we have

$$\begin{aligned} & \mathcal{Q}_{\alpha_t}(\mathbf{V}_{t+1}, \mathbf{z}_t) - \text{Tr}(\mathbf{C}\mathbf{V}_\star) \\ & \leq (1 - \gamma_t \cdot \delta) \left( \mathcal{Q}_{\alpha_t}(\mathbf{V}_t, \mathbf{z}_t) - \text{Tr}(\mathbf{C}\mathbf{V}_\star) \right) - \gamma_t \cdot \delta \cdot \frac{\alpha_t}{2} \|\mathcal{L}\mathbf{V}_t - \mathbf{v}\|^2 + O\left(\alpha_t \gamma_t^2 + \frac{\xi_t \gamma_t}{\sqrt{t}}\right) \end{aligned} \quad (68)$$

Note that

$$\mathcal{Q}_{\alpha_t}(\mathbf{V}_t, \mathbf{z}_t) = \mathcal{Q}_{\alpha_{t-1}}(\mathbf{V}_t, \mathbf{z}_t) + \frac{\alpha_t - \alpha_{t-1}}{2} \|\mathcal{L}\mathbf{V}_t - \mathbf{v}\|^2 \quad (69)$$

Hence

$$\begin{aligned} & \mathcal{Q}_{\alpha_t}(\mathbf{V}_{t+1}, \mathbf{z}_t) - \text{Tr}(\mathbf{C}\mathbf{V}_\star) \\ & \leq (1 - \gamma_t \cdot \delta) \left( \mathcal{Q}_{\alpha_{t-1}}(\mathbf{V}_t, \mathbf{z}_t) - \text{Tr}(\mathbf{C}\mathbf{V}_\star) \right) + ((1 - \gamma_t \cdot \delta)(\alpha_t - \alpha_{t-1})/2 - \gamma_t \cdot \delta \cdot \frac{\alpha_t}{2}) \|\mathcal{L}\mathbf{V}_t - \mathbf{v}\|^2 + O\left(\alpha_t \gamma_t^2 + \frac{\xi_t \gamma_t}{\sqrt{t}}\right) \end{aligned} \quad (70)$$

By choosing  $\gamma_i = \frac{2}{\delta \cdot (i+1)}$  and  $\alpha_i = \alpha_0 \sqrt{\delta i + 1}$ , we claim that

$$(1 - \gamma_t \cdot \delta)(\alpha_t - \alpha_{t-1}) - \frac{\gamma_t \alpha_t}{2} \cdot \delta \leq 0. \quad (71)$$

To verify this, first observe that

$$1 - \gamma_t \delta = \frac{t-1}{t+1}, \quad \alpha_t - \alpha_{t-1} = \alpha_0 \frac{\delta}{\sqrt{\delta t + 1} + \sqrt{\delta(t-1) + 1}}. \quad (72)$$

The LHS becomes:

$$\frac{\alpha_0}{t+1} \left( \frac{(t-1)\delta}{\sqrt{\delta t + 1} + \sqrt{\delta(t-1) + 1}} - \sqrt{\delta t + 1} \right) \quad (73)$$

$$= \frac{\alpha_0}{t+1} \left( \frac{-\delta - 1 - \sqrt{(\delta t + 1)(\delta(t-1) + 1)}}{\sqrt{\delta t + 1} + \sqrt{\delta(t-1) + 1}} \right) \leq 0 \quad (74)$$

Similar as [45], we can obtain the following bound:

$$\mathcal{Q}_{\alpha_t}(\mathbf{V}_{t+1}, \mathbf{z}_{t+1}) - \text{Tr}(\mathbf{C}\mathbf{V}_\star) \leq (1 - \gamma_t \cdot \delta) \left( \mathcal{Q}_{\alpha_{t-1}}(\mathbf{V}_t, \mathbf{z}_t) - \text{Tr}(\mathbf{C}\mathbf{V}_\star) \right) + O\left(\alpha_t \gamma_t^2 + \frac{\xi_t \gamma_t}{\sqrt{t}}\right). \quad (75)$$

Define the error  $e_t = \mathcal{Q}_{\alpha_{t-1}}(\mathbf{V}_t, \mathbf{z}_t) - \text{Tr}(\mathbf{C}\mathbf{V}_\star)$ . The recursion becomes:

$$e_{t+1} \leq (1 - \gamma_t \delta) e_t + O\left(\alpha_t \gamma_t^2 + \frac{\xi_t \gamma_t}{\sqrt{t}}\right). \quad (76)$$

Note that the terms:

- $1 - \gamma_t \delta = 1 - \frac{2}{t+1} = \frac{t-1}{t+1}$ .
- $\alpha_t \gamma_t^2 = \alpha_0 \sqrt{\delta t + 1} \cdot \frac{4}{\delta^2 (t+1)^2} \sim \frac{4\alpha_0}{\delta^{3/2}} t^{-3/2}$ .
- $\frac{\varepsilon \gamma_t}{\sqrt{t}} = \varepsilon \cdot \frac{2}{\delta(t+1)} \cdot \frac{1}{\sqrt{t}} \sim \frac{2\varepsilon}{\delta} t^{-3/2}$ .
- Total perturbation:  $O\left(\left(\frac{4\alpha_0}{\delta^{3/2}} + \frac{2\varepsilon}{\delta}\right) t^{-3/2}\right)$ .

Iterate the inequality:

$$e_{t+1} \leq \prod_{s=1}^t (1 - \gamma_s \delta) e_1 + \sum_{s=1}^t \left[ \prod_{k=s+1}^t (1 - \gamma_k \delta) \right] O \left( \alpha_s \gamma_s^2 + \frac{\xi_s \gamma_s}{\sqrt{s}} \right) \quad (77)$$

$$= O \left( \frac{4\alpha_0}{\delta^{3/2} t^{1/2}} \right) + O \left( \frac{2}{\delta t^2} \cdot \underbrace{\sum_{s=1}^t \xi_s s^{1/2}}_{S(t)} \right). \quad (78)$$

For the additive error term,

$$\mathbb{E}[S(t)] \leq \sum_{s=1}^t \varepsilon s^{1/2} = O(\varepsilon t^{3/2}). \quad (79)$$

According to Chebyshev's inequality,

$$\mathbb{P}(S(t) \geq \mathbb{E}[S(t)] + \varepsilon t^{3/2}) \leq \frac{\text{Var}[S(t)]}{\varepsilon^2 t^3} \leq \frac{\max \text{Var}[\xi_s]}{\varepsilon^2 t}. \quad (80)$$

Therefore

$$\mathbb{E}[e_t] = O \left( \frac{4\alpha_0}{\delta^{3/2} t^{1/2}} + \frac{2\varepsilon}{\delta} \right) \quad (81)$$

and

$$\mathbb{P} \left[ e_t = O \left( \frac{4\alpha_0}{\delta^{3/2} t^{1/2}} + \frac{2\varepsilon}{\delta} \right) \right] \geq 1 - \frac{\max \text{Var}[\xi_s]}{\varepsilon^2 t}. \quad (82)$$

Consequently,

$$\mathbb{P}[\lim_{t \rightarrow \infty} e_t = 0] = 1.$$

Similar to the proof in [45],

$$\mathcal{Q}_{\alpha_t}(\mathbf{V}_{T+1}, \mathbf{z}_{T+1}) \geq \text{Tr}(\mathbf{C}\mathbf{V}_{T+1}) - \frac{D^2}{2\alpha_t}, \quad (83)$$

we then have

$$\text{Objective-gap}_T = \text{Tr}(\mathbf{C}\mathbf{V}_{T+1}) - \text{Tr}(\mathbf{C}\mathbf{V}_*) = O \left( \frac{(1 + \varepsilon)}{\delta^{3/2} \sqrt{T}} \right) \quad (84)$$

For the infeasibility bound, the proof is similar as [45], we can derive the following bound:

$$\text{Infeasibility}_T = \|\mathcal{L}\mathbf{V}_{T+1} - \mathbf{v}\| = O \left( \frac{(1 + \varepsilon)}{\delta^{3/2} \sqrt{T}} \right). \quad (85)$$

□

## D Analysis of Total Error Due to Truncation

The energy function of the Ising model is given by:

$$E[\sigma | J_{ij}, h_i] = - \sum_{i < j} J_{ij} \sigma_i \sigma_j - \sum_i h_i \sigma_i. \quad (86)$$

The objective function of QUBO model is

$$f(\mathbf{x}|q_{ij}) = \sum_{i \neq j} q_{ij} x_i x_j + \sum_i q_i x_i. \quad (87)$$

Let  $\sigma^*$  be the optimal configurations under origin Ising coefficients  $J_{ij}$ s and  $h_i$ s,  $\mathbf{x}^*$  be the corresponding optimal solution to the QUBO model with origin QUBO coefficients  $q_{ij}$ s and  $q_i$ s. We use  $\sigma^{*'}$  to denote the optimal configurations under truncated Ising coefficients, and let  $\mathbf{x}^{*'}$  be the corresponding solution in QUBO model. Then we have the following conclusion

**Lemma 3** *If the Ising coefficients are truncated to  $d$  bits, the error due to truncation is in the order of*

$$\Delta \text{Hamiltonian} = |E[\sigma|J_{ij}, h_i] - E[\sigma^{*'}|J_{ij}, h_i]| = O(2^{-d} \cdot n^2), \quad (88)$$

$$\Delta \text{QUBO Value} = |f(\mathbf{x}|q_{ij}) - f(\mathbf{x}^{*' }|q_{ij})| = O(2^{-d} \cdot n^2). \quad (89)$$

**Proof:** The change in the Ising coefficients due to truncations is

$$|J_{ij} - J'_{ij}|, |h_i - h'_i| = O(2^{-d}), \quad (90)$$

consequently for any  $\sigma$

$$|E[\sigma|J_{ij}, h_i] - E[\sigma|J'_{ij}, h'_i]| = O(2^{-d} \cdot n^2). \quad (91)$$

Note that

$$\begin{aligned} E[\sigma^{*'}|J_{ij}, h_i] &\leq E[\sigma^{*'}|J'_{ij}, h'_i] + O(2^{-d} \cdot n^2) \\ &\leq E[\sigma^*|J'_{ij}, h'_i] + O(2^{-d} \cdot n^2), \end{aligned} \quad (92)$$

and

$$\begin{aligned} E[\sigma^{*'}|J_{ij}, h_i] &\geq E[\sigma^*|J_{ij}, h_i] \\ &\geq E[\sigma^*|J'_{ij}, h'_i] - O(2^{-d} \cdot n^2), \end{aligned} \quad (93)$$

we can obtain (88) by combining (92) and (93).

To convert the Ising model to the QUBO model, we replace the spin variables  $\sigma_i$  with binary variables  $x_i$ , by using the following equation:

$$\sigma_i = 2x_i - 1 \quad (94)$$

Substitute this into the Ising model energy function:

$$E = - \sum_{i < j} J_{ij} (2x_i - 1)(2x_j - 1) - \sum_i h_i (2x_i - 1) \quad (95)$$

$$= - \sum_{i < j} J_{ij} [4x_i x_j - 2x_i - 2x_j + 1] - \sum_i h_i [2x_i - 1] \quad (96)$$

$$= - \sum_{i < j} 4J_{ij} x_i x_j + \sum_i (2 \sum_{j \neq i} J_{ij} - 2h_i) x_i - \sum_{i < j} J_{ij} + \sum_i h_i. \quad (97)$$

Hence  $E[\sigma|J_{ij}, h_i] = f(\mathbf{x}|q_{ij}) + (\sum_i h_i - \sum_{i < j} J_{ij})$  and

$$\Delta \text{QUBO Value} = \Delta \text{Hamiltonian} + O(2^{-d} \cdot n^2) = O(2^{-d} \cdot n^2). \quad (98)$$

When  $d = \Omega(\log n)$ , the additive error is in the order of  $O(\frac{1}{\sqrt{t}})$  for all  $t \leq T$ , and thus the convergence follows from Proposition 1.  $\square$

## E Additional Details of Experimental Results

The training set consists of 12000 images (6000 coat and 6,000 sandal images), and the test set consists of 2000 images (1000 coat and 1000 sandal images). Each image is divided into 3 columns vertically, resulting in two  $28 \times 9$  grid and one  $28 \times 10$  grid. We then calculate the number of zero pixels in each column and use two threshold values to determine the values in a length-3 vector for each image. This vector represents the image as  $-1$ ,  $0$ , or  $1$ , based on the comparison with the thresholds.

A neural network with a hidden layer of depth 1, width 2, and the *Sigmoid* activation function  $\sigma(x) = \frac{1}{1+e^{-x}}$  is used for classification. We approximate the sigmoid activation function with a piecewise constant function. The breakpoints in this experiment is  $\{-8, -4, 0, 4, 8\}$  and the value of the piecewise linear function in each interval is equal to the function value of sigmoid function at the midpoint of that interval.

## F Principles of STE and BinaryConnect

### Straight-Through Estimator (STE) [47, 55]

The Straight-Through Estimator (STE) enables gradient-based training for non-differentiable operations, such as quantization, in neural networks. During the forward pass, a weight  $x_i$  is quantized as:

$$\hat{x}_i = s \cdot \text{clamp}\left(\left\lfloor \frac{x_i}{s} \right\rfloor, n, p\right), \quad (99)$$

where  $s$  is a scaling factor,  $\text{clamp}(\cdot)$  ensures the quantized value lies within integer bounds  $n = q_{\min}/s$  and  $p = q_{\max}/s$ , and the rounding operation  $\lfloor \cdot \rfloor$  is non-differentiable. STE approximates the gradient of the rounding operation as 1:

$$\frac{\partial[\omega]}{\partial\omega} = 1. \quad (100)$$

This allows the gradient to “pass through” the non-differentiable operation, enabling backpropagation for quantized neural networks.

### BinaryConnect [48]

BinaryConnect trains neural networks with binary weights, to reduce computational and memory costs. It maintains real-valued weights  $w$  during training, which are binarized during the forward and backward passes using the sign function:

$$w_b = \text{sign}(w), \quad (101)$$

where  $w_b \in \{-1, +1\}$ . In the forward pass, binary weights  $w_b$  are used to compute activations. In the backward pass, the gradient of the loss  $C$  with respect to the binary weights,  $\frac{\partial C}{\partial w_b}$ , is computed and used to update the real-valued weights. This allows BinaryConnect to accumulate gradient updates in the real-valued weights while operating with binary weights.

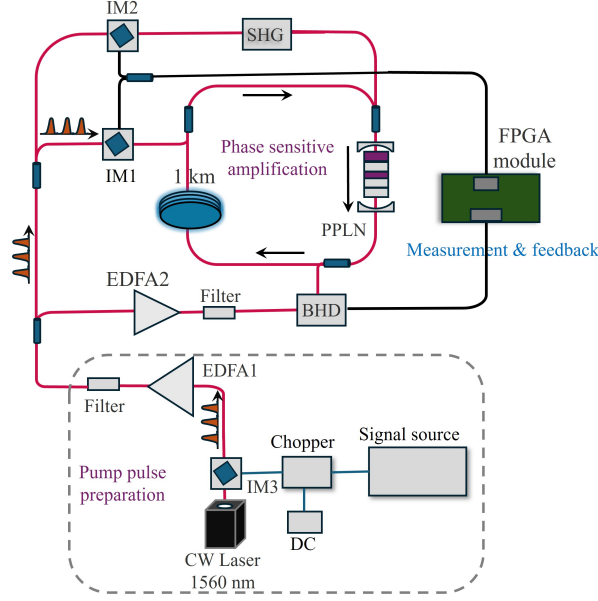


Figure 6: Schematic of the coherent Ising machine (CIM) structure, utilizing optical parametric oscillators and phase-sensitive amplification to solve optimization problems.

## Coherent Ising Machine

As shown in Figure 6, we implement the CIM, an optical system engineered to address combinatorial optimization problems through optical parametric oscillators (OPOs). A continuous wave (CW) laser at 1560 nm initiates the process, feeding into a pump pulse preparation stage. Here, intensity modulators (IM1, IM2, IM3), erbium-doped fiber amplifiers (EDFA1, EDFA2), and filters shape and amplify the light into pump pulses. These pulses enter a second harmonic generation (SHG) unit, producing a frequency-doubled signal, which is then directed into a periodically poled lithium niobate (PPLN) crystal. The PPLN facilitates phase-sensitive amplification, forming a degenerate OPO that generates coherent signal and idler photons. These photons are measured via balanced homodyne detection (BHD), with an FPGA module providing feedback to steer the system toward optimal solutions by mapping the problem onto the Ising model’s energy landscape.

CIM operates by simulating the Ising Hamiltonian, defined as

$$H = - \sum_{i,j} J_{ij} \sigma_i \sigma_j - \sum_i h_i \sigma_i, \quad (102)$$

where  $\sigma_i \in \{1, -1\}$  represents spins,  $J_{ij}$  denotes coupling strengths, and  $h_i$  accounts for external fields. In the PPLN crystal, pump pulses drive parametric amplification, creating optical pulses that encode the spins as two possible phase states. The BHD measures the pulses’ phase and amplitude, determining the system’s energy state. The FPGA uses this data to adjust parameters like pump intensity, effectively minimizing the Hamiltonian through feedback. A chopper and intensity modulators ensure stable pulse circulation in the loop, while the feedback introduces coupling between pulses, mimicking the  $J_{ij} \sigma_i \sigma_j$  interaction terms.

The system’s dynamics allow it to explore the Ising energy landscape efficiently. The optical pulses evolve in parallel, with their interactions governed by the feedback loop, driving the system toward the ground state of the Hamiltonian, which corresponds to the optimization problem’s solution. The amplifiers and filters maintain pulse quality, while the PPLN’s nonlinear efficiency ensures robust signal generation. The BHD’s noise suppression enhances measurement precision, enabling the CIM to handle complex problems by leveraging the coherence and parallelism of optical signals.